ORIGINAL PAPER

Automated detection and measurement of volcanic cloud growth: towards a robust estimate of mass flux, mass loading and eruption duration

Adele Bear-Crozier[1] · Solène Pouget[2] · Marcus Bursik[2] · Emile Jansons[1] · Jarrad Denman[1] · Andrew Tupper[2] · Rose Rustowicz[2]

Abstract

Identifying the spatial extent of volcanic ash clouds in the atmosphere and forecasting their direction and speed of movement has important implications for the safety of the aviation industry, community preparedness and disaster response at ground level. Nine regional Volcanic Ash Advisory Centres were established worldwide to detect, track and forecast the movement of volcanic ash clouds and provide advice to en route aircraft and other aviation assets potentially exposed to the hazards of volcanic ash. In the absence of timely ground observations, an ability to promptly detect the presence and distribution of volcanic ash generated by an eruption and predict the spatial and temporal dispersion of the resulting volcanic cloud is critical. This process relies greatly on the heavily manual task of monitoring remotely sensed satellite imagery and estimating the eruption source parameters (e.g. mass loading and plume height) needed to run dispersion models. An approach for automating the quick and efficient processing of next generation satellite imagery (big data) as it is generated, for the presence of volcanic clouds, without any constraint on the meteorological conditions, (i.e. obscuration by meteorological cloud) would be an asset to efforts in this space. An automated statistics and physics-based algorithm, the Automated Probabilistic Eruption Surveillance algorithm is presented here for auto-detecting volcanic clouds in satellite imagery and distinguishing them from meteorological cloud in near real time. Coupled with a gravity current model of early cloud growth, which uses the area of the volcanic cloud as the basis for mass measurements, the mass flux of particles into the volcanic cloud is estimated as a function of time, thus quantitatively characterising the evolution of the eruption, and allowing for rapid estimation of source parameters used in volcanic ash transport and dispersion models.

Keywords Volcanic cloud · Mass eruption rate · Cloud area · Gravity current · Automated plume detection · Operational tool

---

✉ Adele Bear-Crozier
  Adele.Crozier@bom.gov.au

Extended author information available on the last page of the article

1 Introduction

Identifying the spatial extent of volcanic ash clouds in the atmosphere and forecasting their direction and speed of movement has important implications for the safety of aviation industry assets (i.e. aircraft and aerodromes), community preparedness and disaster management response at ground level. Nine regional Volcanic Ash Advisory Centres (VAACs) were established worldwide to detect, track and forecast the movement of volcanic ash clouds and provide advice to en route aircraft and other aviation assets potentially exposed to the hazards of volcanic ash. VAACs primarily use meteorological satellite systems (both geostationary and polar orbiting) for monitoring volcanic ash cloud occurrence and distribution. The VAAC Darwin area of responsibility extends southward from 20 N and 82 E to 100 E and southward from 10 N and 100 E to 160 E and includes the volcanically active regions of Indonesia, Papua New Guinea, the southern Philippines and west of the Solomon Islands (Fig. 1).

The Japan Meteorological Agency's (JMA) next generation geostationary satellite, Himawari-8, is located 35,793 km above the equator at a longitude of 140.8° E and allows for 10-min temporal and 0.5–2 km spatial resolution retrievals over all volcanoes within the VAAC Darwin area of responsibility. Manual processing of satellite imagery in search of volcanic clouds is time consuming, and thus automated algorithms for detecting volcanic ash clouds and deriving important source term parameters (e.g. estimating growth rate, mass flux, height etc.) are increasingly in demand. However, few such algorithms can deal with the tropical meteorological conditions observed in the VAAC Darwin area of responsibility, in which there are complex, persistent cloud patterns and frequent unstable atmospheric conditions. This problem is exacerbated in regions with a high density of active volcanoes. Both these conditions characterise Central America, upper South America and Southeast Asia. Southeast Asia is particularly vulnerable, given the corresponding high density of air routes (Fig. 1).

In the present contribution, we describe an operational framework to automatically process satellite retrievals and probabilistically identify volcanic clouds. The framework is coupled with a model of near-source volcanic cloud growth based on gravity current behaviour, to gain knowledge of an ongoing eruption, retrieve needed eruption source parameters (ESP) such as the mass eruption rate (MER) and accurately forecast ash dispersion in the atmosphere.
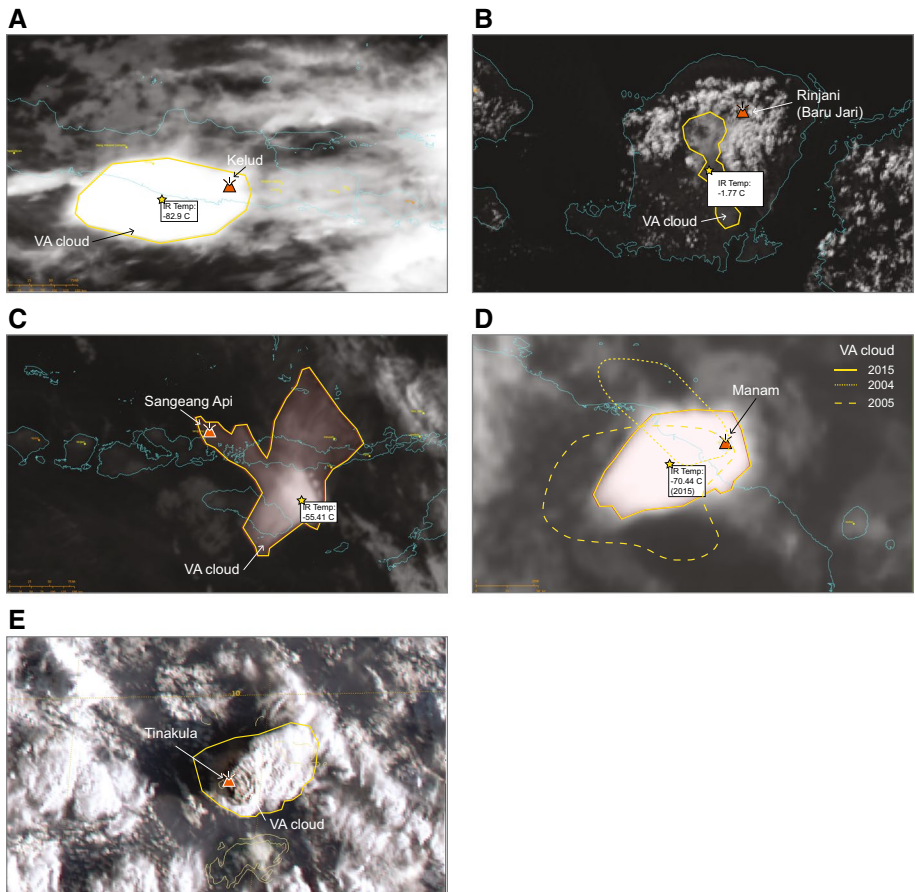
2 Eruption case studies

Eight eruptive events of varying style, duration and intensity that occurred during a range of meteorological conditions are used to perform the analysis. Both radially spreading umbrella clouds and downwind plumes are considered (Fig. 2). volcanic ash advisories (VAAs) are issued in feet due to the requirements of the aviation industry; however, plume heights are described here in metric units.

2.1 Kelud, East Java, Indonesia (13 February 2014)

Kelud is a stratovolcano located in the province of East Java, Indonesia (7.93 °S and 112.308 °E) with a summit height of 1731 m (Global Volcanism Program 2013a; Fig. 1). Kelud has experienced some of the deadliest eruptions in Indonesia. There have been at
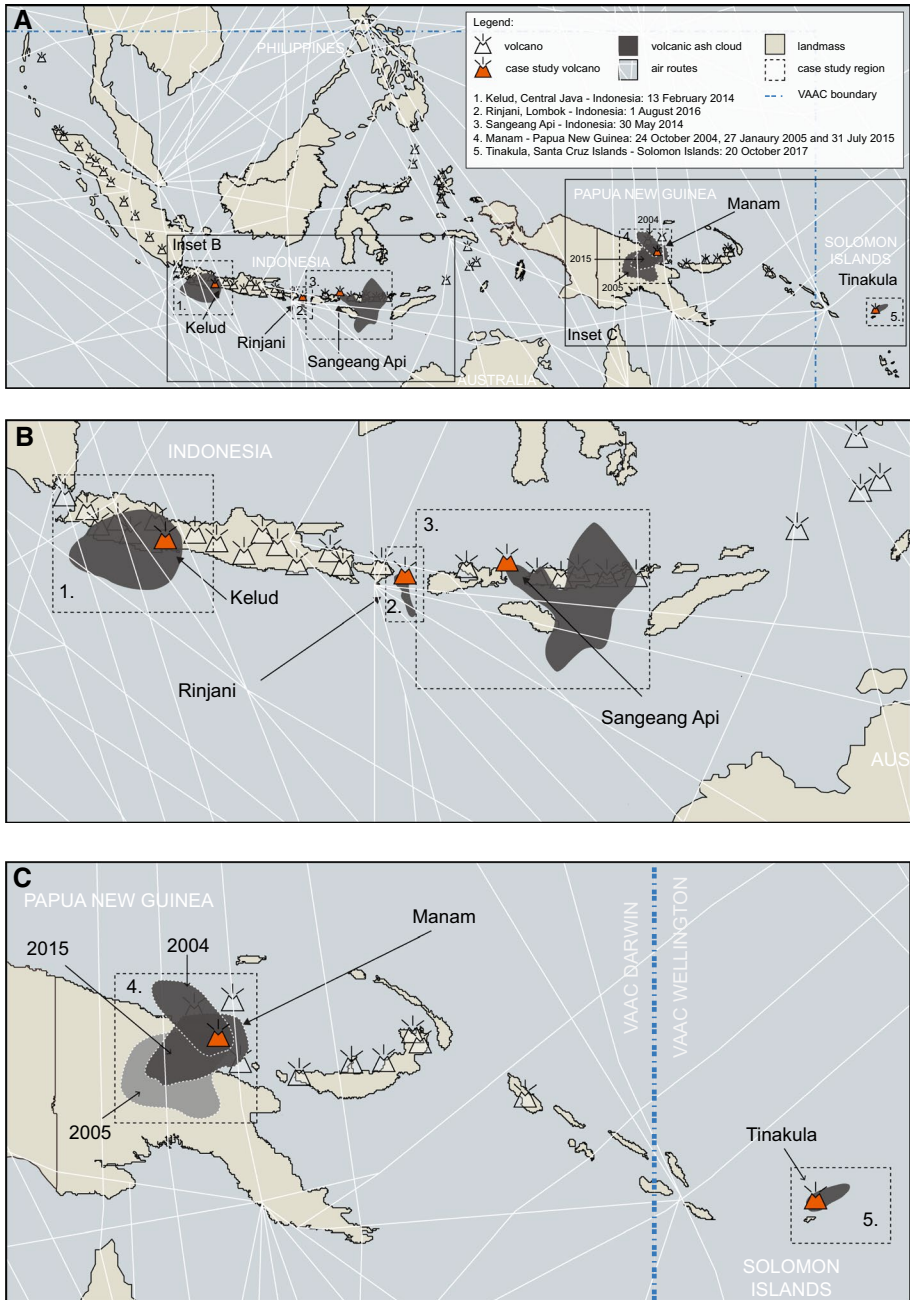
Fig. 1 **a** Schematic map of the five eruption case study volcanoes within the VAAC Darwin area of responsibility overlain by commercial air routes (white) which traverse the region; **b** Zoomed in view of Indonesian case study eruptions [1. Kelud, East Java, Indonesia (13 February 2014); 2. Rinjani, Lombok, Indonesia (1 August 2016) and 3. Sangeang Api, Lesser Sunda Islands, Indonesia (30 May 2014)]; **c** Zoomed in view of Papua New Guinea and South Pacific case study eruptions 4. Manam, Papua New Guinea (24 October 2004), (27 January 2005) and (31 July 2015); and Tinakula, Santa Cruz Islands, Solomon Islands (20 October 2017)

Fig. 2 Satellite imagery of eruption case studies: **a** Kelud; **b** Rinjani (Baru Jari); **c** Sangeang Api; **d** Manam [2004, 2005, 2015 (imagery)] and **e** Tinakula

least 35 explosive eruptions since 1000 AD cumulatively resulting in more than 15,000 deaths (Global Volcanism Program 2013a). At 1415 UTC on 13 February 2014 the Centre for Volcanology and Geo-Hazard Mitigation (CVGHM; Indonesia's national agency for volcano monitoring) reported the ground alert level for Kelud had been raised to four (on a scale of 1 to 4). Visitors and residents were prohibited from approaching the crater within a 10 km radius. Approximately 2 h later (1615 UTC) Kelud experienced a major explosive eruption (Kristiansen et al. 2015). VAAC Darwin closely monitored the evolution of the eruption using MTSAT-2 satellite imagery (VAAC Darwin 2014a). During the first 3 h, the eruptive plume grew into a large umbrella cloud wherein gravity waves were seen. The plume reached a maximum altitude of 26 km (observed on CALIOP lidar) and a spreading altitude of around 16–17 km (Kristiansen et al. 2015). Tephra fallout at ground level (5–8 cm in diameter) caused structures in East Java to collapse, including schools, homes and businesses.

2.2 Rinjani (Baru Jari), Lombok, Indonesia (1 August 2016)

Rinjani is a stratovolcano complex with a maximum height of 3726 m [the second highest in Indonesia; 8.42 °S and 116.47 °E; Global Volcanism Program (2013b)]. The Rinjani volcanic complex is located on the island of Lombok in Indonesia approximately 140 km northeast of Denpasar, a major international aerodrome and hub for aviation assets across the region (Fig. 1). The complex consists of a steep-sided conical shaped stratovolcano (Samalas) truncated by a large caldera feature (Sengara Anak). The western half of the intracaldera region contains a volcanic lake and a post-caldera volcanic cone, Baru Jari, which is the active vent (Global Volcanism Program 2013b). An explosive volcanic eruption occurred at Baru Jari 0400 UTC on 1 August 2016. Aircraft in the immediate vicinity of Lombok reported an initial plume height up to 9.7 km above sea level. VAAC Darwin confirmed volcanic ash detection on Himawari-8 visible satellite imagery moving south and southwest from the vent to an estimated height of 4267–6096 m above sea level. The eruption was characterised by a continuous steady emission of volcanic ash and steam, which ceased after approximately 2 h. The resulting volcanic ash cloud was dispersed south-south-westwards in response to prevailing meteorological conditions and remained observable on Himawari-8 imagery for several hours following the cessation of eruptive activity. Volcanic ash was last observed by VAAC Darwin approximately 230 km to the south-west of Rinjani at 2130 UTC on 1 August 2016.

2.3 Sangeang Api, Lesser Sunda Islands, Indonesia (30 May 2014)

Sangeang Api is a volcanic complex located in the Flores Sea off the northeast coast of Sumbawa, Indonesia (8.2 °S and 119.07 °E; Global Volcanism Program 2013c; Fig. 1). The volcanic complex consists of a caldera containing two large intracaldera cones, Doro Api (1949 m) and Doro Mantoi (1795 m; Global Volcanism Program 2013e). It is one of the most active volcanoes in the Lesser Sunda Islands. On 30 May at 0755 UTC an explosive eruption occurred at Sangeang Api (VAAC Darwin 2014b). At 0832 UTC VAAC Darwin discerned the eruption on MTSAT-2 satellite imagery to a height of approximately 15 km. The ash cloud from the initial explosive eruption separated from the volcano between satellite acquisitions 0832 and 0932 UTC and rapidly moved southeast towards the northern coastline of Australia (Darwin) under the influence of a strong upper tropospheric trough. Following the initial eruption to 15 km, lower level activity was observed at the source for several hours as the optically think core was dispersed to the southeast. By 1500 UTC on 2 June volcanic ash from the event was no longer discernible on satellite imagery (VAAC Darwin 2014b).

2.4 Manam, Papua New Guinea

Manam volcano, located on the island of the same name, is a 1807 m high basaltic-andesitic stratovolcano located 13 km off the northern coast of Papua New Guinea (4.08 °S and 145.037 °E; Global Volcanism Program 2013d; Fig. 1). The summit is surrounded by four radial valleys, which have served as conduits for effusive and pyroclastic material to reach the coast during past eruptions. Manam is one of PNG's most active volcanoes with frequent eruptions of mild to moderate scale recorded during historically over the last 10,000 years. Manam has produced eruptions up to Volcano Explosivity Index 4 (VEI 4) with plumes typically extending high into the stratosphere. Three eruptions at Manam over

the past 14 years which had varying implications for aviation operations in the region are considered here.

2.4.1 October 24, 2004

On 24 October 2004, Manam entered a phase of eruptive activity characterised by several eruptions over a 3-month period (end of January, 2005). The first eruption on 24 October started at 2325 UTC and was classified a strong Strombolian to sub-Plinian eruption, which damaged several villages and a nearby volcano observatory (Tupper et al. 2007). The eruption resulted in an estimated 18 to 22.5 km-high plume affected by a strong wind shear and ensuing pyroclastic flow activity (Tupper et al. 2007). The complex wind situation, the absence of fine-ash fallout layers (indicating a dilute ash cloud) and the effects of meteorological clouds made initial volcanic cloud identification a challenge for VAAC Darwin forecasters using remote sensing techniques (Pavolonis et al. 2006).

2.4.2 January 27, 2005

The strongest eruption in the satellite record for Manam volcano occurred on 27 January 2005, at 1400 UTC (Christie et al. 2005). This eruption was characterised as sub-Plinian to Plinian in style and featured an eruption duration of approximately 2 h. It resulted in the creation of an umbrella cloud, which reached an altitude of approximately 21 to 24 km above sea level (Tupper et al. 2007). A series of five satellite images acquired in 1-h increments from 1325 UTC by a geostationary satellite were used to assess the evolution of the cloud with time. The eruption occurred overnight, and therefore only the infrared band was used and extensive cloud from an active monsoon period was present during the day further complicating retrievals.

2.4.3 July 31, 2015

At approximately 0200 UTC on 31 July 2015 VAAC Darwin received a pilot report for a large eruption underway at Manam (VAAC Darwin 2015). Following inspection of the Himawari-8 (10 min) satellite imagery, VAAC Darwin were able to confirm a significant eruption was occurring and a Volcanic Ash Advisory (VAA) to the aviation industry was issued for volcanic as extending to 13.7 km above sea level. Further analysis confirmed that the volcanic ash plume had reached stratospheric height and the VAA was revised upwards to 19.8 km above sea level (VAAC Darwin 2015). Volcanic ash was observed moving south-southwest and as time progressed the stratospheric height volcanic ash to the south began to dissipate. Lower atmospheric level volcanic ash that was observed initially to a height of 10.7 km and later observed to decrease in height to 4.5 km as it dispersed over the PNG highlands region overnight. On the morning of 1 August, the height of the lower level volcanic ash plume still attached to the volcano was revised upwards to 6.7 km based on satellite imagery analysis. Pilot reports received by VAAC Darwin from aircraft flying through the Highlands region indicated that volcanic ash was visible to aircraft in the area but was no longer discernible on satellite imagery. A continual retraction of the distal extent of the remaining lower level plume back towards the volcano was observed until the eruption ceased on 1 August 2015 at 1820 UTC (VAAC Darwin 2015).

2.5 Tinakula, Santa Cruz Islands, Solomon Islands (20–21 October 2017)

Tinakula is a stratovolcano located in the Santa Cruz Islands, Solomon Islands (VAAC Wellington area of responsibility) with a summit height of 796 m (10.386 °S and 165.804 °E; Global Volcanism Program 2013e; Fig. 1). Tinakula is characterised by a 3.5 km wide island representing the exposed summit of a massive stratovolcano that rises three to four kilometres from the seafloor at the northwest end of the Santa Cruz islands. Eruptions have been frequently observed since 1595 (Global Volcanism Program 2013e). In 1840, an explosive eruption apparently produced pyroclastic flows that completely inundated the surface of the island, killing all of the inhabitants. Frequent more recent eruptions have originated from a volcanic cone constructed within the large breached crater (Global Volcanism Program 2013e). On 20 October at 1920 UTC an eruption occurred at Tinakula. Based on Himawari-8 satellite imagery and observations from ground-based observers, the initial pulse (Tinakula 1) rose to a maximum height of 15 km above sea level. A second eruptive pulse (Tinakula 2) occurred at 2350 UTC, which generated a plume to 16.6 km above sea level.

3 Satellite imagery analysis

Data on cloud dimensions and temperatures were extracted from satellite imagery and are documented in Appendices 1 and 2 of ESM. Maximum and minimum cloud temperatures were found to be near the cloud edge, and centre of mass, respectively, in most images (Fig. 2). In general, the minimum temperature increased with time, indicating a thinning of cloud, while the maximum temperature stayed approximately constant. The clouds of the case studies spread in different fashions. The clouds of both Kelud and Manam spread as somewhat elongated umbrella clouds that both began as approximately axisymmetric, then evolved to an oval or elliptical shape. The cloud of Sangeang Api stayed roughly equant, but the outline was highly irregular. The clouds of Rinjani and Tinakula all evolved to highly elongated shapes, consistent with development of downwind plumes. These clouds thus represent a spectrum of the different potential and typical dispersion patterns commonly associated with volcanic cloud in the VAAC Darwin (and Wellington) areas of responsibility.

3.1 Human operator

Quantitative data on cloud shape were determined manually by a skilled observer (Pouget) or a volcanologist (Bear-Crozier). Clouds were outlined; then cloud areas and cross sections were measured, as well as minimum and maximum brightness temperatures. An automated volcanic plume detection algorithm was also considered herein to detect and delineate the boundary extents of the Kelud, Manam 2004 and Manam 2005 volcanic clouds. These datasets can be used to compare with the forecaster characterisation of the cloud in order to test how an algorithm differs from an expert operator.

3.2 Automated Probabilistic Eruption Surveillance (APES)

The Automated Probabilistic Eruption Surveillance (APES) algorithm is an experimental identification system that is documented here. The algorithm requires a set of at least four

consecutive NetCDF satellite images with latitude, longitude and spectral radiance, as well as a representative atmospheric temperature and wind profile. This can be obtained from a radiosonde (observed meteorology) or Numerical Weather Prediction (NWP; modelled meteorology). Currently the algorithm runs for approximately 16 s to process four images on a regular desktop computer. APES consists of three key processes, convective analysis, image processing and determination of eruptive clouds. These processes are described below and graphically depicted in the flow chart in Fig. 3.

3.2.1 Convective analysis

The Convective Available Potential Energy (CAPE), the mixing level, the equilibrium level and the location of temperature inversions are initially calculated to estimate the levels where clouds are likely to form. For tropical areas, there are typically two main inversions identified: the low-level trade wind inversion and the Tropopause. These are levels of resistance to buoyant cloud ascent; typically, a layer of cumulus will be associated with the low-level inversion; and thunderstorm activity will be trapped beneath the Tropopause. Secondary cloud families such as TS-derived cirrus and altocumulus are also common.

From the CAPE analysis, the algorithm derives:

- The expected number of cloud layers.
- The heights of the expected cloud layers.
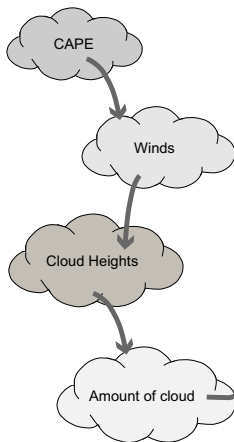- The steering winds averaged across each of the layers.

3.2.2 Image processing
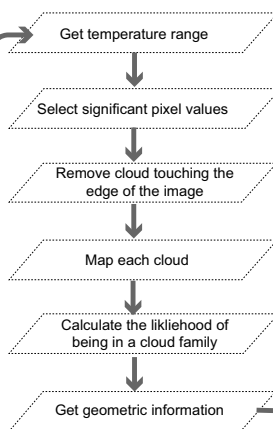
The image analysis step is divided in two main parts:

1. Calculation of the image thresholds; and

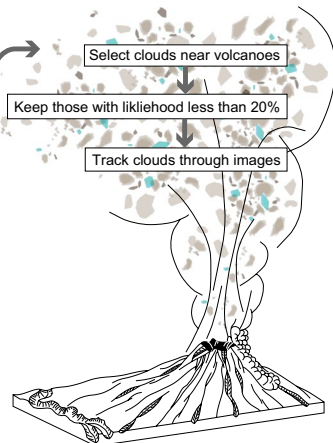**AUTOMATED PROBABILISTIC ERUPTION SURVEILLANCE (APES)**

Fig. 3 Schematic diagram of the convective analysis, image processing and determination of eruptive cloud processes which characterise the Automated Probabilistic Eruption Surveillance (APES) algorithm

2.   The image sequence processing.

The image thresholds represent the conversion of the spectral radiance array into an interval of values between 0 and 1, referred to as pixel values. Thus, we obtain images with values indicating a temperature range (i.e. 0 for the warmest pixels, and 1 the coldest pixels). The statistical distribution of pixel values in each image is then determined to be able to calculate and apply a 1-sigma Gaussian smoothing function, following which the pixel values of the N most significant peaks are extracted. This way, a representative pixel value for each of the N cloud levels identified is determined by applying a distance-based clustering algorithm to the peak values from the past three images. As a result, the average of the largest N clusters is used as the thresholds in the current image.

Once this is done, the image sequence can be processed to gain information about the different cloud groups. This is achieved by mapping the contour of each of the N image thresholds, fitting polygons to each closed region of the image contours, discarding any polygon touching the edge of the image.
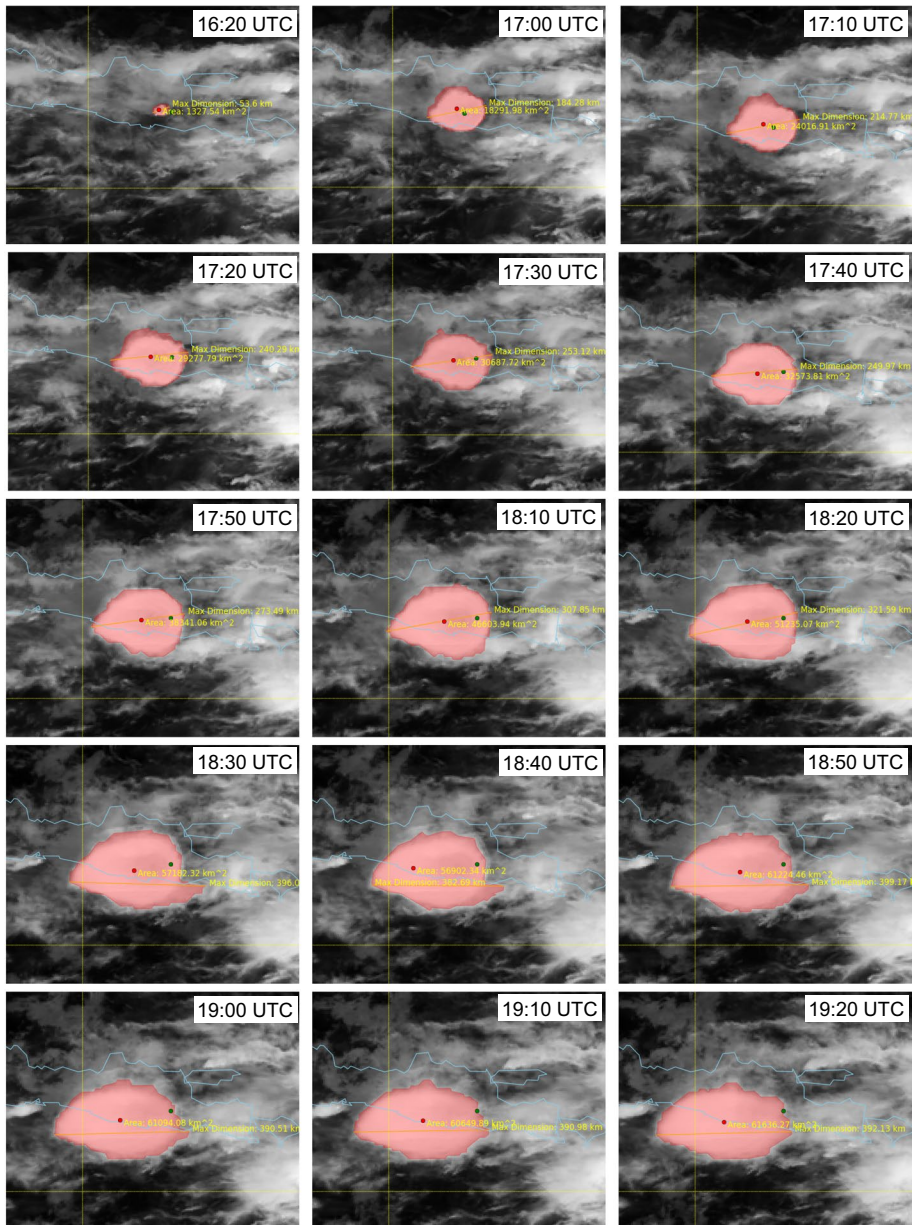
3.2.3 Determination of eruptive clouds

The third step involves identification of the volcanic cloud. This is achieved by repeating the first two processes on a new image for already existing cloud families as well as newly identified cloud families.

By considering the geographical location of volcanoes, a cloud created near a volcano will be flagged as a potential eruptive cloud. To assess the potential of this cloud to be volcanic, the probability of each eruptive cloud candidate being representative of an existing cloud family is calculated, and if the likelihood is determined to be less than 20%, the cloud is labelled as being an eruptive cloud and will be put in the eruptive cloud family. The image thresholds and population statistics are recalculated based on the latest retrieval and the process continues. Once an eruption has been identified the cloud is tracked in each successive retrieval (Fig. 4). Brightness temperature, area, centre of mass and other parameters are tracked.

3.2.4 Determination of eruptive cloud diameters

An additional algorithm was developed to automatically determine an eruptive cloud's shortest and longest diameters. These extreme diameters are useful in determining whether the eruptive cloud is an umbrella cloud or downwind plume and in calculating the growth rate.

To determine the eruptive cloud diameters, an input cloud mask is used, as derived from the previous algorithm. The cloud mask is an image of white and black pixels, where the cloud pixels are white and all others are black. The centre of mass of the cloud is determined as an (x, y) pixel location. After identifying the (x, y) pixel locations of each pixel on the boundary between the white cloud and the black background, all radii are calculated as Euclidean distances between the location of the centre of mass and the locations of each boundary contour pixel. To determine diameters, the angle between each radius connecting the centre of mass and each boundary pixel is computed. Two radii that are closest to 180° from one another are determined to be pairs. The length of each set of pairs is added together to get the cloud diameters.

Fig. 4 Determination of the eruptive cloud growth from Kelud volcano (East Java), Indonesia (red) on 13 February between 1620 UTC and 1920 UTC using the APES algorithm

4 Model of cloud growth

Once the growth of the cloud is measured either by hand or by APES (Appendices 1 and 2 of ESM), the Mass Eruption Rate (MER) is calculated. To estimate the MER of the

plume at the level of intrusion, we used the gravity current models of initial volcanic cloud growth developed by Sparks et al. (1997) for an umbrella cloud, and by Bursik et al. (1992) for a downwind plume. The models were implemented in Pouget et al. (2013). Although the approximations used for the underlying physics have proven difficult to justify (Pouget et al. 2016), they have nevertheless resulted in some good fits to data (Costa et al. 2013).

A vigorous volcanic plume rises from the vent and spreads by the entrainment and expansion of air, and by pressure differences at the cloud front that arise from the difference between the density of the material in the plume, and that in the stratified, ambient atmosphere. At the neutral buoyancy level, entrainment-driven rise is arrested by the positive density anomaly above, and motion becomes dominated by the cloud-front pressure differences, resulting in the growth of the cloud in the horizontal direction (Fig. 5).

We thus model volcanic clouds as initially axisymmetric intrusions of well-mixed fluid into an otherwise quiescent, stratified atmosphere. Early on, as the rising eruption column begins to spread at the neutral buoyancy level, the flow is complex and highly turbulent with several potential mechanisms affecting the rate of spreading, including
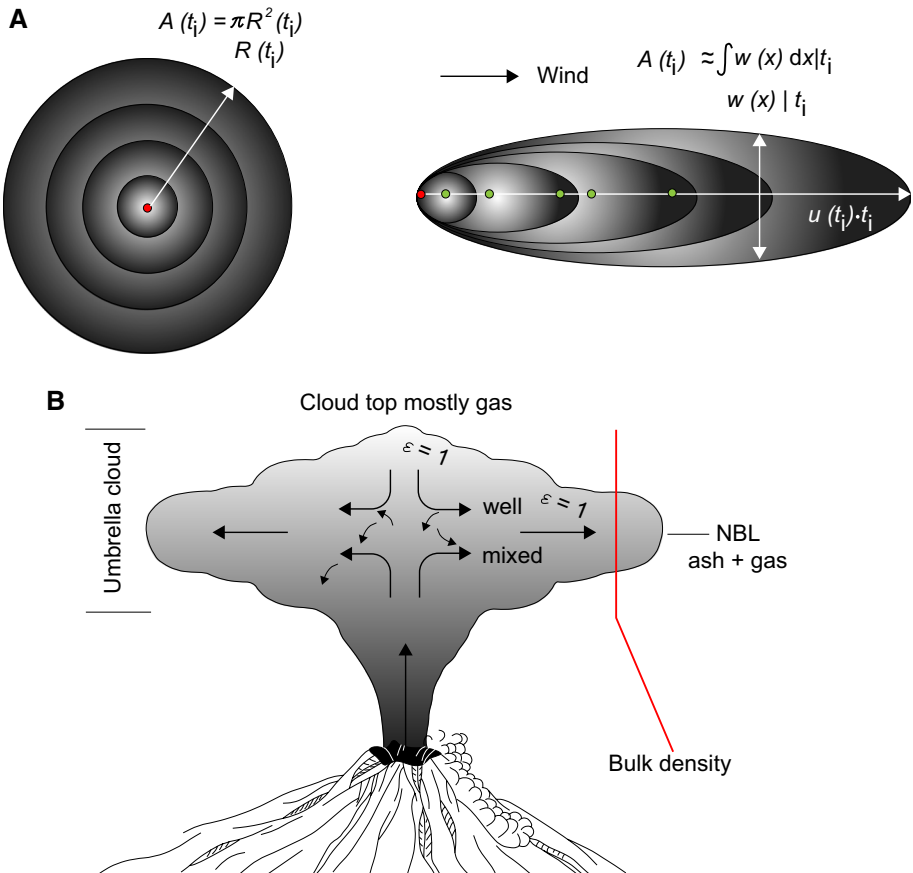
Fig. 5 **a** Schematic representation of plume growth model; **b** schematic representation of gravity and wind-driven plume growth model

momentum-driven flow (Chen 1980; Kotsovinos 2000), resulting from the collapse of plume fluid that has risen above the neutral buoyancy level. This early phase we believe to correspond to an observational 'mushroom' phase or stage, as seen in cloud mapping (Pouget et al. 2016). However, as the cloud spreads, the dynamics become driven by horizontal pressure gradients resulting from variations in the thickness of the intrusion. These pressure gradients are referred to by the more general term 'buoyancy'.

As growth of a vigorous cloud by buoyancy is stopped in the upwind direction at the stagnation point (Carey and Sparks 1986), its spread becomes dominated by wind, of which the horizontal momentum is entrained into the intrusion, and which also applies a traction to the upper and lower surfaces of the cloud. We refer to the resulting windblown plume as a 'strong downwind' plume, as it developed from an umbrella cloud (e.g. Fig. 2a). In less vigorous plumes, rise is arrested by the wind itself, as the entrainment of downwind momentum comes to dominate vertically directed buoyant rise. This leads to growth of what can be called a 'weak downwind' plume (e.g. Fig. 2e), in which downwind transport is *not* at the height of neutral buoyancy in a still atmosphere but is rather at a lower neutral buoyancy level consistent with enhanced entrainment due to wind. The two types of downwind plume can often be distinguished in satellite retrievals, as the weak plume tends to retain a puffy appearance, its turbulence not having been reorganised in the upper atmosphere during gravitational intrusion.

Most studies of the buoyancy-driven spreading mechanism for intrusions are based on a box model, in which a single, characteristic cloud thickness is assumed, allowing equations of motion to be derived using force balances or scaling arguments (Lemckert and Imberger 1993). These approaches lead to the prediction that the radius of a continuously supplied, vigorous plume grows as $t^{2/3}$ (Woods and Kienle 1994), which has become widely used (Sparks et al. 1997; Costa et al. 2013; Pouget et al. 2013). However, it has been argued that the underlying assumption that it is possible to capture the unsteady evolution of the thickness of the cloud through a single characteristic variable is inappropriate (Johnson et al. 2015). Johnson et al. (2015) and Pouget et al. (2016) used a new conceptualisation to perform analytical and numerical modelling of a buoyancy-driven intrusion, which solves a complete system of 'shallow-water' equations to give the evolution of the ash cloud radius with time, as well as its thickness and radial velocity as functions of space and time. This model assumes that the buoyancy-dominated state forms two distinct dynamic regimes, with different behaviour close to the unsteady front from what is observed in the steady interior. Asymptotic solutions at late times are consistent with the radius growing as $t^{3/4}$ in the buoyancy-inertial regime. Full numerical solutions allowed these workers to study the transition between different flow regimes as indicated by different asymptotic behaviours, such as the onset of significant drag effects late in spread, as the buoyancy force decreases.

In the present work, we assume the physics is still being resolved, and thus calculate MER according to Pouget et al. (2013) but provide, in our algorithms, tests of the different physical approximations and flow regimes by investigating goodness of fit to different power law curves arising from the different theories. Furthermore, instead of using a sample of radii of the cloud as in Pouget et al. (2013), which were used to approximate the shape of the volcanic cloud at different times (Fig. 5a), the model was modified to use the increasing area of the cloud, which is automatically measured in the APES processing before the radii.

4.1 Gravity and wind-driven plume growth

We review analytical models of the growth of umbrella clouds, and strong and weak downwind plumes in the context of the effects of gravity and wind on increasing cloud area, and how increasing area can be used to estimate MER (umbrella_MER).

4.1.1 Umbrella cloud

An umbrella cloud is an approximately axisymmetric, gravity-driven intrusion into the atmosphere. This phenomenon is the result of spreading at a neutral buoyancy level, either for the entire plume or segregated fractions thereof, with no major effect from wind. The classical development of such intrusive gravity currents uses a box-model approximation (i.e. the cloud is assumed to be shaped in cross section like a rectangle of constant thickness in space and gradually decreasing with time, ΔH, assuming no increase in MER with time). In the case of a continuous release (over more than a few minutes), continuity suggests that:

$$\mathrm{d}(A\Delta H\bar{\rho}) = Q\mathrm{d}t. \tag{1}$$

where A is the planform area of the cloud, $\bar{\rho}$ is the cloud bulk density, Q is total mass flux into the cloud and t is time. We assume that the umbrella cloud grows primarily as an inertial gravity current within a stratified ambient, the speed of advance of the front, U, being a function of the current depth, hence for momentum:

$$U = \lambda N\Delta H \tag{2}$$

where λ is a constant of order unity that could change as the planform shape changes, and N is the Brunt–Vaisala frequency. This momentum equation can be coupled with the continuity equation, Eq. 1, to remove the dependence on cloud thickness (Lemckert and Imberger 1993; Sparks et al. 1997). Following transformation of infinitesimals to simple differences, we obtain for the mass flux into the umbrella cloud at time i, Q_i:

$$Q_i = \frac{2\bar{\rho}}{3\sqrt{\pi}\lambda N}\left(\frac{A_i^{3/2} - A_{i-1}^{3/2}}{t_i^2 - t_{i-1}^2}\right) \tag{3}$$

Following Pouget et al. (2013), we used a value of $\lambda = 1$, although Suzuki and Koyaguchi 2009 found $\lambda = 0.2$ in numerical modelling. The informal sensitivity investigation of Pouget et al. (2013) suggested that a change in the value of λ of 0.1 caused a change in MER estimate of ~5%. Nevertheless, its value is worthy of further investigation. Using this, and integrating between any two times t_{i-1} and t_i, assuming quasisteady cloud growth, the volumetric growth rate at time i can thus be expressed as a function of planform cloud area (Eq. 3).

In the case of an instantaneous release (over a few seconds to a few minutes), in which the intrusion timescale >> eruption timescale:

$$V = \pi r^2 \Delta H = \text{constant} \tag{4}$$

so:

$$V = A \frac{\mathrm{d}(A/\pi)^{1/2}}{\lambda N \mathrm{d}t} \tag{5}$$

and, as a result after transformation from infinitesimals to simple differences, the mass in the cloud estimated at time i, m_i, becomes:

$$m_i = \frac{2\bar{\rho}}{3\sqrt{\pi}\lambda N} \left(\frac{A_i^{\frac{3}{2}} - A_{i-1}^{\frac{3}{2}}}{t_i - t_{i-1}} \right) \tag{6}$$

4.1.2 Downwind plume

A downwind plume of strong or weak type occurs when the wind distorts the volcanic cloud into an elongated shape with long axis in the downwind direction. For intense eruptions, the downwind plume can be followed over hundreds of kilometres [e.g. the downwind plume from the climactic Mount St Helens (18 May 1980) could be followed for about 1100 km (Bursik et al. 1992)]. For a weak plume, the downwind plume may persist over only a few kilometres (Sparks et al. 1997). In either case, assuming the cloud is fed from the vent during downwind growth (instantaneous release would result in detachment from the vent), the area of the plume at any time is given by:

$$A_i = \int r(x)\mathrm{d}x|_{t=t_i} \tag{7}$$

where $r(x)$ is width of the downwind plume as a function of downwind distance, x. Width increases by gravity (i.e. in the downwind direction, the plume elongates by wind, but its width increases by gravity current flow). Following Bursik et al. (1992), for momentum:

$$\frac{\mathrm{d}r}{\mathrm{d}t} = \frac{\mathrm{d}r}{\mathrm{d}x}\frac{\mathrm{d}x}{\mathrm{d}t} = \frac{\mathrm{d}r}{\mathrm{d}x}u = \lambda' N \Delta H \tag{8}$$

where u is wind speed and $\lambda' \sim 0.85$ is a constant related to the shape of the cloud. By continuity:

$$Q = \bar{\rho} r(x) u \Delta H \tag{9}$$

where $\bar{\rho}$ is bulk density of the volcanic cloud. So, substituting the expression for ΔH from Eq. (9) into Eq. (8), then integrating that, and solving for r, we can obtain (Bursik et al. 1992):

$$r(x) = \left(\frac{2\lambda' NQx}{u^2} \right)^{1/2} \tag{10}$$

Note that for weak downwind plumes, crosswind growth is dominated by entrainment; hence, it cannot directly yield an estimate of MER. Taking the derivative with respect to time of Eq. (7), substituting for r from Eq. (10), integrating, rearranging and taking finite differences, we find:

$$Q_i = \frac{9\bar{\rho}}{8\lambda'\text{Nu}} \frac{\left(A_i^2 - A_{i-1}^2\right)}{\left(t_i^3 - t_{i-1}^3\right)} \tag{11}$$

The maximum and minimum cloud diameters are compared to determine whether the eruptive cloud is an umbrella cloud or a downwind plume. The premise being that in an umbrella cloud, the difference between the maximum and minimum diameters is relatively small, whereas in a downwind plume, this difference is relatively large. Expressed as the ratio of the maximum to the minimum diameter, a threshold value of max/min > 3 is used to indicate a downwind plume.

Following Pouget et al. (2013), the mean bulk density, $\bar{\rho}(H_\text{b})$, of the material in the umbrella cloud or downwind plume was estimated to be the same as that of the atmosphere at the height of the lowest sensed, highest temperature (outermost) part of the cloud, H_b, assuming the cloud to be a gravitational intrusion at the neutral buoyancy level, and to be thermally opaque (Fig. 5b). It was calculated using the brightness temperature at the edge of the cloud and comparing this with the temperature in an atmospheric sounding and finding the corresponding pressure. The mean bulk density in the intrusion is then given by the ideal gas law:

$$\bar{\rho}(H_\text{b}) = P(H_\text{b})/\left(T_\text{b}(H_\text{b})R_\text{d}\right) \tag{12}$$

where P is pressure, T_b is the brightness temperature and R_d is the gas constant for dry air, assuming the cloud to be sufficiently dilute. Similarly, the density of the gas alone in the cloud, ρ_g, is estimated using the lowest brightness temperature (highest part of cloud) and the pressure at that height from radiosonde or NWP data. This assumes that near the cloud top, the cloud is gas alone due to incipient gas-ash separation (Holasek et al. 1996; Prata et al. 2017).

The MER of the particles at the level of intrusion, i.e. into the intrusion, is $Q_{i,\text{p}} = \pi\rho_\text{p}R_{H_\text{b}}^2 u_{H\text{b}}$, where ρ_p is the particle field density, $R_{H\text{b}}$ is the radius at H_b and $u_{H\text{b}}$ is the mean (upward) speed of material into the umbrella cloud. Then, the particle mass flux can then be estimated from the MER of the cloud at the level of intrusion, $Q_{i,H\text{b}} = \pi\bar{\rho}R_{H_\text{b}}^2 u_{H_\text{b}}$, since $Q_{i,H\text{b}}/\bar{\rho} = Q_{i,\text{p}}/\rho_\text{p}$ and $\bar{\rho} \equiv \rho_\text{p} + \rho_\text{g}$ so that:

$$Q_{i,\text{p}} = Q_{i,H_\text{b}}\left(1 - \rho_\text{g}/\bar{\rho}\right) \tag{13}$$

The particulate masses, in the case of instantaneous intrusions, are calculated using a cognate equation for the particle and cloud masse, respectively.

4.2 Other models of MER

Models of plume rise height or column height are typically used to estimate MER. The simplest, and most commonly used, is the *empirical method*, first introduced by Wilson et al. (1978), and modified since by Sparks et al. (1997) and Mastin et al. (2009). This model is based on the notion that plume rise is primarily controlled by MER, and that atmospheric conditions yield some or all of the uncertainty in that first-order estimate. This assumption is largely borne out by the data, and nevertheless, there can be large anomalies produced by wind and atmospheric moisture, making a trustworthy estimate dependent on an accurate atmospheric sounding. In the moist tropics (VAAC Darwin area), normal atmospheric convection typically reaches altitudes of 17–18 km (due to a high tropopause

and abundant moisture), and both modelling, and observations suggest that in some cases, quite minor eruptions can also trigger deep volcanic convection (Tupper et al. 2009). Empirical techniques that neglect tropopause height variation and atmospheric moisture are, in general, most likely to suffer from the associated uncertainties and to overestimate MER.

Many numerical models of plume rise have been introduced, which take into consideration the atmospheric sounding (Costa et al. 2016). In the present contribution, we use two of these—Plumeria (Mastin et al. 2014) and PlumeRise (Woodhouse et al. 2013), which are readily available through the web, and produce output that can be compared to that from umbrella_MER. The online, web version of PlumeRise and the FORTRAN90 version of Plumeria with incorporation of wind entrainment were used.

5 Results

Estimated MER (kg s^{-1}) values and associated plume height time series for each event considered are detailed in Table 1 and average MER estimates by technique are summarised in Table 2. All cloud parameterisation inputs, meteorological inputs and volcanological inputs used are documented in Appendices 1–4 of ESM. Example outputs are shown in Figs. 6 and 7. Figure 6 shows an example of the output to screen for one of the case study eruptions presented here (Tinakula I). Note in particular the last section, which summarises the information on the eruption as determined from the behaviour of the eruption cloud, including total mass erupted and eruption duration. These are critical parameters for incorporation into ash dispersal models. Figure 7 displays examples of the growth of the cloud area on satellite imagery and includes power law curve fits for comparison with different physical models of cloud growth. Detailed discussion of these models and curve fits is beyond the scope of the present contribution, but cf. Pouget et al. (2016) for a thorough discussion and evaluation. Figure 7 also shows examples of cumulative mass of ash erupted into the umbrella cloud as a function of time. In the next subsections, we will concentrate on the MER results for the different eruptions, as MER and cloud height are the two primary pieces of information to produce quantitative, concentration based outputs of cloud movement for evaluation in aviation safety. Here, we note that the data on long-term cloud growth investigated herein (Fig. 7) support convergence of all clouds to turbulent drag behaviour, consistent with expectation (Pouget et al. 2016).

5.1 Kelud, East Java, Indonesia (13 February 2014)

Estimated MER (kg s^{-1}) values for the 13 February (2014) eruption of Kelud are plotted in Fig. 8a. MER estimates for each model are plotted in 60 min increments over a 7-h period that volcanic ash cloud dimensions remained clearly discernible on MTSAT-2 satellite imagery. The average MER for each model varies from a low of 3.97E+06 kg s^{-1} (Plumeria) to a high of 4.42E+07 kg s^{-1} (umbrella_MER; Tables 1 and 2). The average MER returned by PlumeRise and the empirical method were intermediate between these two models (1.16E+07 kg s^{-1}) and 1.45E+06 kg s^{-1}, respectively (Tables 1 and 2). Estimates of MER for the initial detection timestep (i.e. time of initial detection, $T+0$, to $T+1$ h) vary between models from 2.17E+06 kg s^{-1} (Plumeria) to 1.18E+07 kg s^{-1} (Empirical method) with PlumeRise intermediate between the two at 7.76E+07 kg s^{-1}. The empirical method and PlumeRise estimates of MER follow a similar trend over time,

Table 1 Mass eruption rate (MER) estimations for each case study eruption for each model (PlumeRise, empirical method, umbrella_MER and Plumeria) including plume height time series data

Time (UTC)	Plume height (m)	PlumeRise	Empirical	umbrella_MER	Plumeria
Kelud, Central Java (Indonesia)—13 February 2014					
16:30	15,343	7.76E+06	1.18E+07	–	2.17E+06
17:00	–	–	–	1.63E+08	–
17:10	–	–	–	1.69E+07	–
17:20	–	–	–	5.86E+07	–
17:30	16,331	1.26E+07	1.52E+07	1.57E+06	4.10E+06
17:40	–	–	–	2.03E+06	–
17:50	–	–	–	6.21E+06	–
18:10	–	–	–	9.24E+07	–
18:20	–	–	–	2.58E+07	–
18:30	16,585	1.41E+07	1.62E+07	6.51E+07	4.81E+06
18:40	–	–	–	–	–
18:50	–	–	–	4.54E+07	–
19:00	–	–	–	–	–
19:10	–	–	–	–	–
19:20	–	–	–	9.39E+06	–
19:30	16,585	1.41E+07	1.62E+07	–	4.81E+06
20:30	16,585	1.41E+07	1.62E+07	–	–
21:30	16,378	1.28E+07	1.54E+07	–	–
22:30	15,852	1.00E+07	1.35E+07	–	–
23:30	15,185	7.21E+06	1.13E+07	–	–
Rinjani, Lombok (Indonesia)—1 August 2016					
3:50	5547	4.12E+04	1.72E+05	1.52E+06	8.870E+04
4:00	6439	9.08E+04	3.20E+05	1.52E+06	1.290E+05
4:10	6792	1.63E+05	4.00E+05	1.32E+06	1.510E+05
4:20	6908	1.25E+05	4.29E+05	1.42E+06	1.580E+05
4:30	6986	1.32E+05	4.49E+05	6.53E+05	1.630E+05
4:40	6812	1.79E+05	4.05E+05	2.07E+07	1.520E+05
4:50	6695	1.09E+05	3.76E+05	7.60E+06	1.430E+05
5:00	6381	8.70E+04	3.08E+05	9.11E+06	1.260E+05
5:10	6026	6.52E+04	2.43E+05	5.58E+06	1.080E+05
5:20	5368	3.37E+04	1.50E+05	1.48E+06	8.210E+04
Sangeang Api (Indonesia)—30 May 2014					
8:32	–	–	–	–	–
Instantaneous eruption					
Manam (Papua New Guinea)—31 July 2015					
1:32	13,724	4.62E+06	7.40E+06	1.43E+08	7.520E+05
2:32	15,042	6.62E+06	1.08E+07	1.43E+08	1.79E+06
3:32	14,252	4.98E+06	8.66E+06	1.35E+08	1.11E+06
4:32	12,856	4.06E+06	5.64E+06	1.94E+08	4.02E+05
Tinakula 1 (Solomon Islands)—20 October 2017					
19:30	15,097	9.69E+06	1.10E+07	4.30E+07	1.78E+06
20:20	16,600	1.22E+07	1.63E+07	4.30E+07	3.41E+06
20:30	16,600	1.22E+07	1.63E+07	1.25E+07	3.41E+06

Table 1 (continued)

Time (UTC)	Plume height (m)	PlumeRise	Empirical	umbrella_MER	Plumeria
20:40	16,600	1.22E+07	1.63E+07	1.68E+07	3.41E+06
20:50	16,600	1.22E+07	1.63E+07	1.46E+07	3.41E+06
21:00	16,600	1.22E+07	1.63E+07	1.65E+07	3.41E+06
21:30	16,600	1.22E+07	1.63E+07	1.34E+07	3.41E+06
21:50	17,412	1.84E+07	1.99E+07	2.23E+07	5.16E+06
22:10	15,097	9.69E+06	1.10E+07	4.99E+07	1.78E+06
22:20	14,866	9.21E+06	1.03E+07	9.64E+06	1.63E+06
22:40	14,180	8.28E+06	8.48E+06	4.30E+06	1.24E+06
22:50	14,180	8.28E+06	8.48E+06	–	1.24E+06
Tinakula 2 (Solomon Islands)—20 October 2017					
23:50	16,600	1.22E+07	1.63E+07	9.69E+07	3.41E+06
0:10	16,600	1.22E+07	1.63E+07	9.69E+07	3.41E+06
0:20	16,600	1.22E+07	1.63E+07	3.39E+07	3.41E+06
0:30	16,600	1.22E+07	1.63E+07	2.33E+07	3.41E+06
0:40	16,600	1.22E+07	1.63E+07	1.52E+07	3.41E+06
1:10	16,600	1.22E+07	1.63E+07	1.37E+07	3.41E+06
1:30	16,146	1.27E+07	1.45E+07	5.90E+06	2.75E+06
1:50	15,724	1.13E+07	1.30E+07	4.70E+06	2.30E+06
Manam (Papua New Guinea)—24 October 2004					
0:25	18,500	1.96E+07	2.56E+07	2.51E+07	1.230E+07
1:25	18,500	1.96E+07	2.56E+07	1.08E+07	1.230E+07
2:25	18,500	1.96E+07	2.56E+07	1.65E+07	1.230E+07
3:25	18,500	1.96E+07	2.56E+07	0.00E+00	1.230E+07
4:25	18,500	1.96E+07	2.56E+07	1.37E+06	1.230E+07
Manam (Papua New Guinea)—27 January 2005					
15:25	24,000	1.35E+08	7.53E+07	5.37E+08	7.750E+07
16:25	24,000	1.35E+08	7.53E+07	2.22E+08	7.750E+07
17:25	24,000	1.35E+08	7.53E+07	1.35E+08	7.750E+07

peaking at 1.62E+07 kg s^{-1} (Empirical method) and 1.41E+07 kg s^{-1} (PlumeRise) at $T+3$ h. Both the empirical method and PlumeRise estimates then decrease incrementally. Estimates for Plumeria are lower than the empirical method and PlumeRise estimates peaking at 4.81E+06 kg s^{-1} at $T+2$ h before following a typically decreasing trend over time. For Kelud, we estimated MER using umbrella_MER from both manual and algorithmic cloud edge definition. Estimates based on algorithmic cloud edge definition follow a pulsatory increasing and decreasing trend over time with a maximum MER of 1.63E+08 kg s^{-1} (Fig. 8a). Umbrella_MER results based on manual cloud edge definition yielded the highest estimations of MER (e.g. 3.96E+08 kg s^{-1}; Fig. 8a).

5.2 Rinjani (Baru Jari), Lombok, Indonesia (1 August 2016)

Estimated MER (kg s^{-1}) values for the 1 August (2016) eruption of Rinjani are plotted in Fig. 8b. MER estimates for each model are plotted in 10 min increments over the 90-min

Table 2 Average MER estimates for each case study event for each model

Volcano	Location	VAAC region	Event	PlumeRise	Empirical	umbrella_MER	Plumeria
Kelud	Central Java, Idnoensia	VAAC Darwin	13 February 2014	1.16E+07	1.45E+07	4.42E+07	3.97E+06
Rinjani (Baru Jari)	Lombok, Indonesia	VAAC Darwin	1 August 2016	1.03E+05	3.25E+05	6.14E+04	1.30E+05
Sangeang Api	Lesser Sunda Is. Indonesia	VAAC Darwin	30 May 2014	Instantaneous eruption			
Manam	Papua New Guinea	VAAC Darwin	31 July 2015	5.22E+06	8.38E+06	1.57E+06	8.26E+05
Manam	Papua New Guinea	VAAC Darwin	24 October 2004	1.96E+07	2.56E+07	1.34E+07	1.230E+07
Manam	Papua New Guinea	VAAC Darwin	27 January 2005	1.35E+08	7.53E+07	2.98E+08	7.750E+07
Tinakula	Solomon Is.	VAAC Wellington	20 October 2017 (Tinakula 1)	1.14E+07	1.39E+07	1.84E+05	1.49E+07
Tinakula	Solomon Is.	VAAC Wellington	20 October 2017 (Tinakula 2)	1.21E+07	1.57E+07	2.42E+05	3.19E+06

Umbrella_MER/Umbrella_MER-0.5_current/src')
Reloaded modules: get_YODHMS, get_probabilities, write_MER_data, get_info_from_txt, power_fit_coeffs, get_MERs_cloudtype, plot_tss_vs_A, get_N, plot_MER, get_rhos, get_tss
Run time = 2019-12-04 13:49:49.912457
Input file = /Users/mib/Desktop/Documents/Plume/Model/Umbrella_MER/Umbrella_MER-0.5_current/data/Tinakula/test_tinakula_1_ftc.ssv

------------------ Density check ------------------------
Estimated bulk density of cloud = [0.33306562 0.33306562 0.33306562 0.33306562 0.33306562 0.33306562
 0.33306562 0.33306562 0.33306562 0.33306562 0.33306562 0.33306562]
Estimated gas density = [0.22017015 0.17584257 0.17584257 0.17584257 0.17584257 0.17584257
 0.17584257 0.15145435 0.22017015 0.22539172 0.24752455 0.24752455]
----

xxxxxxxxxxxxxxxxxx Cloud growth xxxxxxxxxxxxxxxxxxxxxxxxxxx
Cloud is spreading as an umbrella cloud.
Mass flux ash into cloud = 43034181.7388849 kg/s
Cloud is spreading as an umbrella cloud.
Mass flux ash into cloud = 12509703.962799447 kg/s
Cloud is spreading as an umbrella cloud.
Mass flux ash into cloud = 16765952.007987656 kg/s
Cloud is spreading as an umbrella cloud.
Mass flux ash into cloud = 14574325.791398266 kg/s
Cloud is spreading as an umbrella cloud.
Mass flux ash into cloud = 16530146.746317392 kg/s
Cloud is spreading as an umbrella cloud.
Mass flux ash into cloud = 13379731.677865025 kg/s
Cloud is spreading as a downwind plume.
Mass flux of ash into cloud = 22252158.46465048 kg/s
Cloud is spreading as a downwind plume.
Mass flux of ash into cloud = 49890947.06900294 kg/s
Cloud is spreading as a downwind plume.
Mass flux of ash into cloud = 9644211.148029149 kg/s
Cloud is spreading as a downwind plume.
Mass flux of ash into cloud = 4297305.669215985 kg/s
Dissipating. Eruption stopped.
Mass flux of ash into cloud = 0.0 kg/s
xxxxxxxxxxxxxxxxxxxxxxxxxxxxxxxxxxxxxxxxxxxxxxxxxxxxxxxxxx

****************** Summary information ******************
Tot. mass ash = 286929159474.1742 kg
Est. volume (DRE) = 0.11477166378966967 cu km
MERp(t) = [0.0, 43034181.7388849, 12509703.962799447, 16765952.007987656,
14574325.791398266, 16530146.746317392, 13379731.677865025, 22252158.46465048,
49890947.06900294, 9644211.148029149, 4297305.669215985, 0.0] kg/s
mean MERp = 18443514 +/- 14776016 kg/s
eruption duration = 11400 s
****

Fig. 6 Example output of algorithm for Tinakula 1 cloud. First section: run parameters and statistics. Second section (–): check on gas and bulk density to see if consistent with model assumptions. Third section (xx): Observations of cloud size and geometry, with implied MER. Fourth section (**): summary information, including total mass of ash injected at cloud level and eruption duration
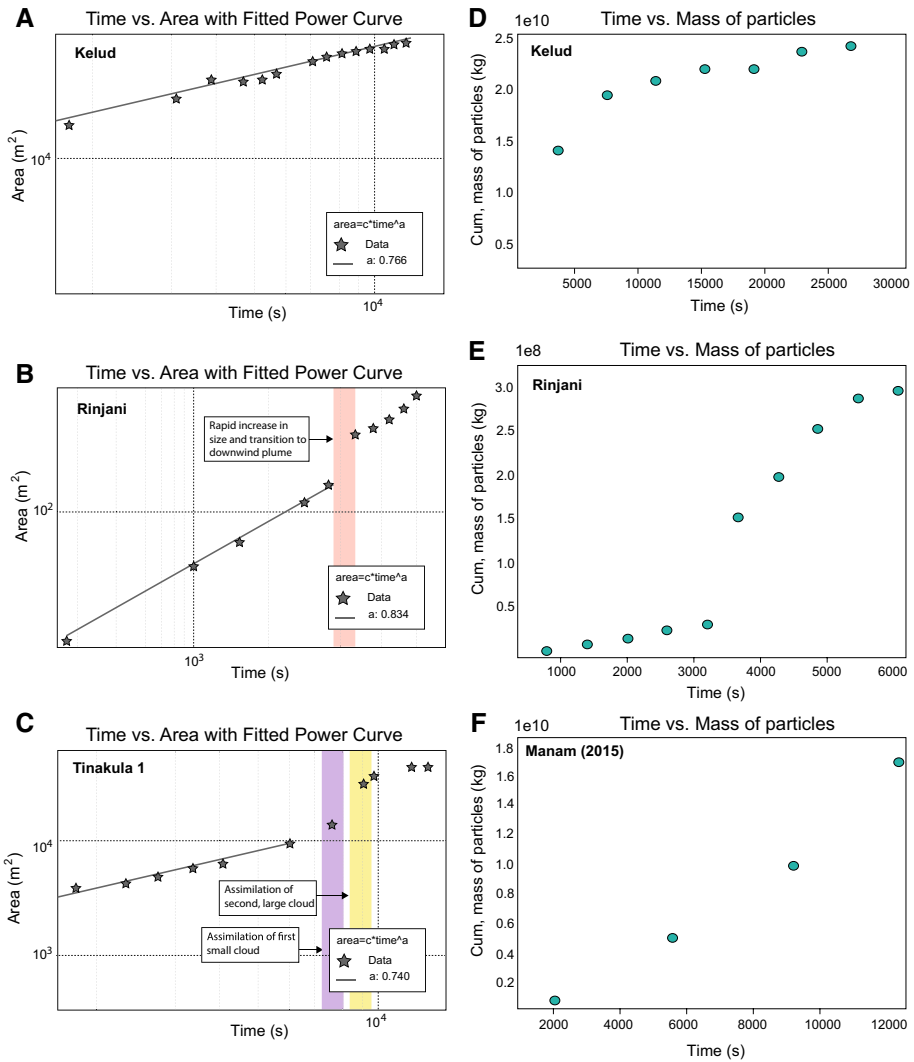
Fig. 7 a Growth of cloud area with time for Kelud (2014); **b** for Rinjani (2016) and; **c** for Tinakula (2017; power law fits to data, with estimated coefficients, a, shown in legend box); **d** cumulative mass flux of particles in volcanic cloud for Kelud (2014); **e** for Rinjani (2016), and **f** for Manam (2015; all plots have first data point at $t = 0$, mass$=0$)

period that volcanic ash cloud dimensions remained clearly discernible on Himawari-8 satellite imagery. The average MER for each model varies from a low of 6.16E+04 kg s^{-1} for umbrella_MER to a high of 3.25E+05 kg s^{-1} for the empirical method, with PlumeRise and Plumeria returning average MERs intermediate between these two models (1.03E+05 and 1.30E+05 kg s^{-1}, respectively; Tables 1 and 2). Estimates of MER for the initial detection timestep (i.e. time of initial detection, $T + 0$, to $T + 10$ min) vary between models from 4.12E+04 (PlumeRise) to 1.72E+05 kg s^{-1} (Empirical method), with estimated MER for Plumeria intermediate between the two values (8.87E+04 kg s^{-1}). The umbrella_MER

Fig. 8 Composite total mass flux (kg s^{-1}) versus time (seconds) charts of each MER estimation technique ▶ for **a** Kelud (2014; incorporating Hargie et al. 2019 estimates for time averaged MER and Maeno et al. 2019 estimated for average MER based on deposit mapping); **b** Rinjani (2016); **c** Sangeang Api (2014); **d** Manam (2015); **e** Manam (2004); **f** Manam (2005); **g** Tinakula (2017—Phase 1) and **h** Tinakula (2017—Phase 2). 'Empirical' implies numerical values of fitting parameters from Mastin (2009)

estimates peak at 2.07E+07 kg s^{-1} at T3600 s. This estimate represents the highest value of all the plume models considered for the Rinjani event. This corresponds to the time of transition from umbrella to downwind plume behaviour, but may be partly at least an artefact of the transition in model.

The umbrella_MER values decrease steadily to 1.48E+06 kg s^{-1} at $T+6000$ s when the dimensions of the plume are no longer clearly discernible on satellite imagery. Plumeria and PlumeRise MER estimates for Rinjani are broadly in agreement throughout the eruption, peaking at 1.63E+05 kg s^{-1} at $T+3000$ s and 1.79E+05 kg s^{-1} at $T+3000$ s, respectively. Plumeria and PlumeRise estimates are characteristically lower than the empirical method estimates for the duration.

5.3 Sangeang Api, Lesser Sunda Islands, Indonesia (30 May 2014)

Analysis of this event showed the volcanic cloud propagating away from the vent between the first and second satellite acquisitions. The eruption of Sangeang Api is therefore considered to be instantaneous, as the eruption had ceased between the first and second retrievals. We thus have no comparison of MER for this event.
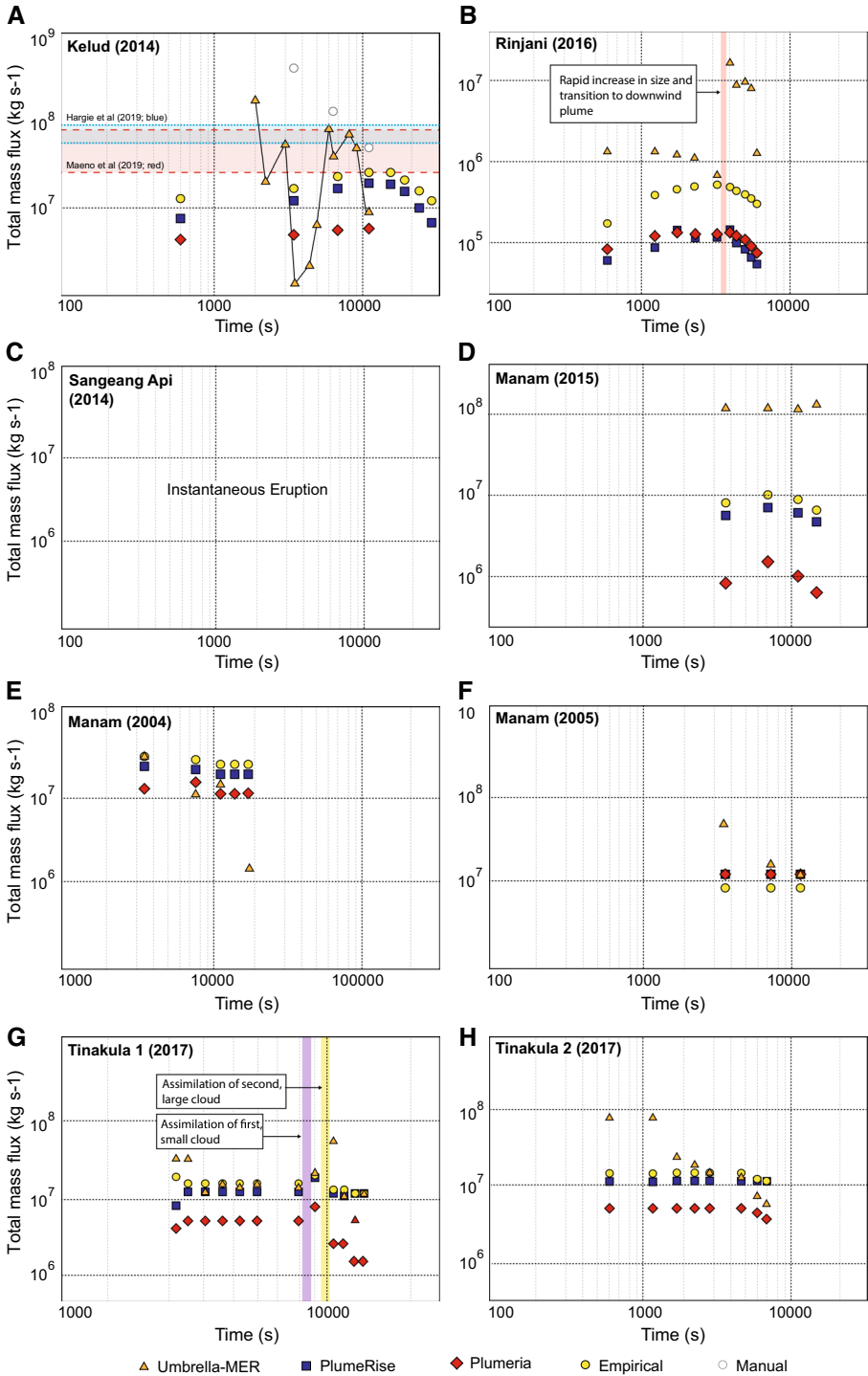
5.4 Manam, Papua New Guinea

5.4.1 July 31, 2015

Estimated MER (kg s^{-1}) values for the 31 July (2015) eruption of Manam are plotted in Fig. 8d. MER estimates for each model are plotted in 60-min increments over a 4-h period that volcanic ash cloud dimensions remained clearly discernible on MTSAT-2 satellite imagery. The average MER for each model varies from a low of 8.26E+05 (Plumeria) to a high of 8.38E+06 kg s^{-1} (empirical method; Tables 1 and 2). PlumeRise and umbrella_ MER returned average MERs intermediate between these two models (5.22E+06 and 1.57E+06 kg s^{-1}, respectively). Estimates of MER for the initial detection timestep (i.e. time of initial detection, $T+0$, to $T+1$ h) vary between models from 7.52E+05 (Plumeria) to 1.43E+08 kg s^{-1} (umbrella_MER) with the estimated MER from PlumeRise and Plumeria intermediate between the two (4.62E+06 and 7.40E+06 kg s^{-1}, respectively). The umbrella_MER estimates of MER peak at 1.94E+08 kg s^{-1} after 3 h. This represents the highest value of all the plume models considered for the Manam 2015 event. Estimates for PlumeRise are characteristically less than those for the empirical method but follow a similar decreasing trend over time. Plumeria estimates are lowest, decreasing steadily with time to low of 4.02E+05 kg s^{-1} at $T+3$ h.

5.4.2 October 24, 2004

Estimated MER (kg s^{-1}) values for the 24 October (2004) eruption of Manam are plotted in Fig. 8e. MER estimates for each model are plotted in 60-min increments over a 4-h period

A **Kelud (2014)**
B **Rinjani (2016)**
C **Sangeang Api (2014)** — Instantaneous Eruption
D **Manam (2015)**
E **Manam (2004)**
F **Manam (2005)**
G **Tinakula 1 (2017)**
H **Tinakula 2 (2017)**

Legend: △ Umbrella-MER   ■ PlumeRise   ◆ Plumeria   ○ Empirical   ○ Manual

that volcanic ash cloud dimensions remained clearly discernible on MTSAT-2 satellite imagery. The average MER for each model varies from a low of 1.23E+07 (Plumeria) to a high of 2.56E+07 kg s^{-1} (empirical method; Tables 1 and 2). The PlumeRise and umbrella_MER methods returned average MER estimates intermedia between the two of 1.96E+07 kg s^{-1} and 1.34E+07 kg s^{-1}. Estimates of MER for the initial detection timestep (i.e. time of initial detection, $T+0$, to $T+1$ h) vary between models from a low of 1.23E+07 kg s^{-1} (Plumeria) to a high of 2.56E+07 kg s^{-1} (empirical method). Estimates for the empirical method remain constant over time (2.56E+07 kg s^{-1}) based on a steady cloud top height of 18.5 km and neutral buoyancy height of 17 km. This represents the highest value of all the plume models considered for the Manam 2004 event. Estimates for all four methods are in reasonably good agreement for the duration of the event with umbrella_MER showing a more rapid decrease to 1.37E+06 kg s^{-1} after $T+3$ h (Fig. 8e).

5.4.3 January 27, 2005

Estimated MER (kg s^{-1}) values for the 27 January (2005) eruption of Manam are plotted in Fig. 8f. MER estimates for each model are plotted in 60 min increments over a 4-h period that volcanic ash cloud dimensions remained clearly discernible on MTSAT-2 satellite imagery. The average MER for each model varies from a low of 7.50E+07 (Plumeria) to a high of 2.98E+08 kg s^{-1} (umbrella_MER; Tables 1 and 2). PlumeRise returned an average MER estimate of 1.35E+08 kg s^{-1}, and the empirical method estimated an average MER of 7.53E+07 kg s^{-1}. Estimates of MER for the initial detection timestep (i.e. time of initial detection, $T+0$, to $T+1$ h) vary between models from a low of 7.50E+07 kg s^{-1} (Plumeria) to a high of 5.37E+08 kg s^{-1} (umbrella_MER), with an estimate of 1.35E+08 kg s^{-1} for PlumeRise and 7.53E+07 kg s^{-1} for the empirical method. Estimates for umbrella_MER peak at 5.37E+08 kg s^{-1} after 1 h. This represents the highest value of all the plume models considered for the Manam 2004 event. Estimates for umbrella_MER steadily decline to a minimum of 1.35E+08 kg s^{-1} at $T+3$ h when the dimensions of the plume are no longer clearly discernible on satellite imagery. Estimates for the all four methods remain reasonably constant over time based on a steady cloud top height of 24 km and neutral buoyancy height of 21 km.

5.5 Tinakula, Santa Cruz Islands, Solomon Islands (20–21 October 2017)

5.5.1 Tinakula 1

Estimated MER (kg s^{-1}) values for the initial pulse of the 20–21 October (2017) eruption of Tinakula (Tinakula 1) are plotted in Fig. 8g. MER estimates for each model are plotted in 10 to 20 min increments over the 2.5 h period that volcanic ash cloud dimensions remained clearly discernible on Himawari-8 satellite imagery. The average MER for each model varies from a low of 1.84E+05 kg s^{-1} for the umbrella_MER to a high of 1.49E+07 kg s^{-1} for the Plumeria with PlumeRise and the empirical method returning average MERs intermediate between these two models (1.14E+07 and 1.39E+07 kg s^{-1}, respectively; Tables 1 and 2). Estimates of MER for the initial detection timestep (i.e. time of initial detection, $T+0$, to $T+10$ min) vary between models from 1.78E+06 kg s^{-1} (Plumeria) to 4.3E+07 kg s^{-1} (umbrella_MER) with the estimated MER from PlumeRise and the empirical method intermediate between the two (9.69E+06 kg s^{-1} and 1.10E+07 kg s^{-1}, respectively). The empirical method estimates remained steady for the

first 60 min of the eruption at 1.63E+07 kg s^{-1} before peaking at 1.99E+07 kg s^{-1} 70 min and gradually declining to 8.48E+06 kg s^{-1}. PlumeRise estimates of MER for Tinakula 1 are broadly constant at 1.22E+07 kg s^{-1} for the first 60 min of the eruption, peaking at 1.84E+07 kg s^{-1} at 70 min before gradually decreasing to 8.28E+06 kg s^{-1}. Estimates from umbrella_MER are high 4.30E+07 kg s^{-1} at the time of initiation before steadily decreasing over the first 2.5 h. Estimate for umbrella_MER rapidly increase after 2.5 h to 4.99E+07 kg s^{-1}, the highest value calculated for Tinakula 1. Estimates for all methods show a gradual decline after 2.5 h.

5.5.2 Tinakula 2

Estimated MER (kg s^{-1}) values for the second pulse of the 20–21 October (2017) eruption of Tinakula (Tinakula 2) are plotted in Fig. 8h. MER estimates for each model are plotted in 10 to 20 min increments over the 100 min period that volcanic ash cloud dimensions remained clearly discernible on Himawari-8 satellite imagery. The average MER for each model varies from a low of 2.42E+05 kg s^{-1} for the umbrella_MER to a high of 1.57E+07 kg s^{-1} for the empirical method with PlumeRise and Plumeria returning average MERs intermediate between these two models (1.21E+07 and 2.19E+06 kg s^{-1}, respectively; Tables 1 and 2). Estimates of MER for the initial detection timestep (i.e. time of initial detection, $T+0$, to $T+10$ min) vary between models from 3.41E+06 (Plumeria) to 9.69E+07 kg s^{-1} (umbrella_MER). Estimates for umbrella_MER peak at 9.69E+07 kg s^{-1} at the time of initiation before gradually reducing to 4.70E+06 kg s^{-1} over the duration of the eruption. Plumeria estimates for Tinakula 2 remain constant for the first 60 min of the eruption before reducing to 2.3E+06 kg s^{-1} during the closing stages of the eruption. The empirical method estimates remained steady for the first 70 min of the eruption at 1.63E+07 kg s^{-1} before gradually declining to 1.30E+07 kg s^{-1}. PlumeRise estimates of MER for Tinakula 2 are broadly constant at 1.22E+07 kg s^{-1} for the first 70 min of the eruption before gradually decreasing to 1.13E+07 kg s^{-1} in the closing stages of the eruption.

6 Discussion

6.1 Comparison between manual and automatic plume outlining

The automatic and manual outlining of the plume yield similar results in terms of the trend of plume growth with time, as indicated by the use of the two methods for the eruption of Kelud (Fig. 8a). Furthermore, more informal comparison of the outlining process and algorithmic results for different eruptions show that they are similar, and the inferences drawn, comparable, with some notable exceptions (discussed in Sect. 6.3). This may be in part because APES models the way in which a human operator differentiates a volcanic cloud from other cloud objects. One subtlety that APES does not capture is the variations in brightness temperature at the cloud edge, which the human operator tends to use. Within each image, APES uses a constant temperature cloud edge, whereas the human operator is able to discern 'dips' in the sensed plume edge. This is consistent with the observation, commonly seen in data from limb sounding instruments that the cloud edge is not at a constant opacity, height or brightness temperature. Alternatively, the constant temperature criterion provides an objective delimiter of the cloud edge. Another thing to be careful

about with the automatic plume detection algorithm is the position of the volcano. If several volcanoes are close to each other (common in the VAAC Darwin area), then false alerts are triggered more often. This is a point we are currently addressing.

6.2 Comparison between the use of radius or area

Although we did not explicitly test for it, comparison of operator and algorithm behaviour and results for calculation of MER showed us that the use of the radius or the area of the cloud yields relatively similar results for the estimation of MER in many cases for the umbrella cloud stage, consistent with the assumption that cloud spread is approximately axisymmetric. However, depending on where the radius is measured, it can lead to an over-estimation or an under-estimation of the MER. Use of area provides a better estimate of MER when few radii are measured. To obviate this problem, either many radii should be used for measurement, or the position of measurement needs to be chosen carefully. Use of many radii could also provide multiple estimates of MER that can then be averaged. We suspect that the most robust method might be to use the area measurement for the mean, and multiple measurements of radius to provide an uncertainty estimate. Similarly, for the downwind plume, multiple downwind distances and downwind plume widths were used by Pouget et al. (2013) in the original implementation. At least superficially, this process could yield a more robust estimate of MER because numerous measurements can be averaged at each time. Using area provides only one measurement per time step. Again, it might be best to use the area measurement for the mean and provide an uncertainty estimate with the multiple measurements at different downwind distances and plume widths.

6.3 Comparison among rise height and umbrella growth models for MER calculation

In a number of cases, MER estimated from umbrella_MER and rise height-based models are similar. However, it is worthwhile to note and discuss the exceptions for each eruption. There are contrasts in both overall, average or systematic behaviour, but there are also differences that are purely local in space or time, that are caused by locally or transiently operating processes. Both types of differences will be addressed in the following. In doing this, it is perhaps useful to outline some general 'Rules of Thumb' for understanding the relationship between the models of MER and the observations. These Rules of Thumb are guidelines for interpretation only and should not be followed slavishly. They can be enumerated thus:

1. umbrella_MER is measured as the mass flux rate directly into the volcanic cloud, whereas the rise height techniques provide estimates of flux from the vent. Thus, umbrella_MER should yield lower values for the mass eruption rate.
2. Water vapour is entrained into the plume as it rises. In a moist atmosphere, the amount of vapour can be so great that its heat content, which is what drives plume rise, is higher than the heat content of the pyroclasts. Thus, a volcanic plume will rise unusually high for a given MER, and over a range of MER, plumes will reach the same altitude limited by the available atmospheric energy (think of thunderheads). In such a case, the empirical method will tend to estimate an MER that is high relative to the other techniques.

3. Following on this point, for a moist atmosphere, Plumeria and PlumeRise should produce outputs that reach approximately the same rise height over a range of values for small MER, since most of the energy to drive the eruption comes from the atmosphere, causing them to estimate MER inaccurately at times. Since a significant part of the buoyancy anomaly is from water, umbrella_MER will tend to overestimate MER. At larger MER, a more straightforward mapping between MER and rise height will exist.
4. PlumeRise and Plumeria include wind entrainment, the empirical method does not, so at a given rise height, the empirical method will yield an estimate of low MER relative to PlumeRise and Plumeria and possibly umbrella_MER.
5. Following on this point, rise height can be the same over a range of (relatively high) MER for PlumeRise and Plumeria in the case of high wind. In this case, eruptions over a range of potentially too high MER values could result in rise to the same height.
6. Finally, it is important to remember that the combination of a moist atmosphere, occasional incurrence of the subtropical jet and the strong cold-point tropopause in the equatorial region provide a powerful tendency for convective phenomena to rise to the tropopause height of c. 15 km. For all eruptions, there is the chance that this provides an additional modulation on and problem for all MER calculations.

In the discussion to follow, we use these 'Rules of Thumb' with discretion as guidelines to understanding MER calculations.

6.3.1 Kelud

For Kelud (Fig. 8a) estimates of MER are all quite consistent. MER was estimated from both manual and algorithmic cloud edge definition (Fig. 8a). The result is that manual definition yields a higher estimated MER, which is almost certainly the result of defining the cloud edge at a higher brightness temperature than does the algorithm. In this sense, these two techniques could provide bounds on estimates of umbrella_MER, as well as results from independent observations. Umbrella_MER estimated MER was 4.4 ± 4.9E+07 kg s^{-1}, which compares well with the 1–2E+07 kg s^{-1} values for the rise height methods, 8–10E+07 kg s^{-1} for the independent umbrella growth estimate of Hargie et al. (2019), and 6.5 ± 2.8E+07 kg s^{-1} values obtained by Maeno (2019) based on deposit mapping (Fig. 8a). Total volume estimated by Maeno et al. (2019) was 0.13–0.26 km^3 DRE, considerably below our estimate of 0.9 km^3 DRE. The MER calculated by umbrella_ MER is considerably more variable than that calculated by the rise height methods, or by Hargie et al. (2019), but this is almost surely the result of slow growth to shrinking observed in APES in the first hour of the eruption, and between 1820 UTC and 1850 UTC as the eruption ceased (Fig. 4). The APES drawn cloud does not appear to have any major shortcomings or inconsistencies, so it is possible that this is a reflection of normal variation in cloud growth rate, and potentially, source mass flux.

6.3.2 Rinjani

For Rinjani (Fig. 8b), umbrella_MER estimates are high relative to the other estimates and increase at c. 3000 s to two orders of magnitude greater. Taking Rule of Thumb (3) into consideration, the generally higher MER estimates by umbrella_MER may be the result of a moist atmosphere, which is a trend that is seen virtually throughout our record in this study. Considering Rule of Thumb (2), this suggestion of a moist atmosphere is

Fig. 9 **a** Himawari-8 retrieval for 0430 UTC during the Rinjani eruption; **b** Himawari-8 retrieval for 0440 ▶ UTC during the Rinjani eruption featuring rapid increase in plume width and length to the south; **c** time versus MER particles for the Rinjani event

consistent with the observation for almost all eruptions in this group of the empirical method yielding MER higher than PlumeRise and Plumeria. The increase at c. 3000 s corresponds to a temporary change in cloud growth exponent, and a transition to downwind plume behaviour (Fig. 7b). Inspection of the satellite imagery shows that at this time, the cloud was interpreted to grow rapidly in width and to the south (Fig. 9). At later times, the growth rate resumed the previous trend. The interpretation is that this may be a case of operator error in not defining the cloud edge from image to image in an evolving situation. An algorithm is clearly helpful in this sense, in applying criteria that are known to be consistent. After this large increase in cloud growth rate, the rate returned to only slightly elevated levels, suggesting that the umbrella cloud and downwind models are somewhat consistent with each other.
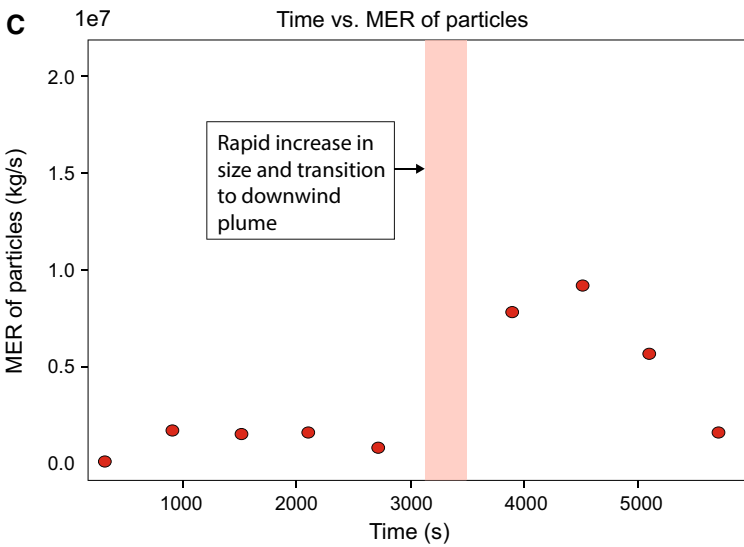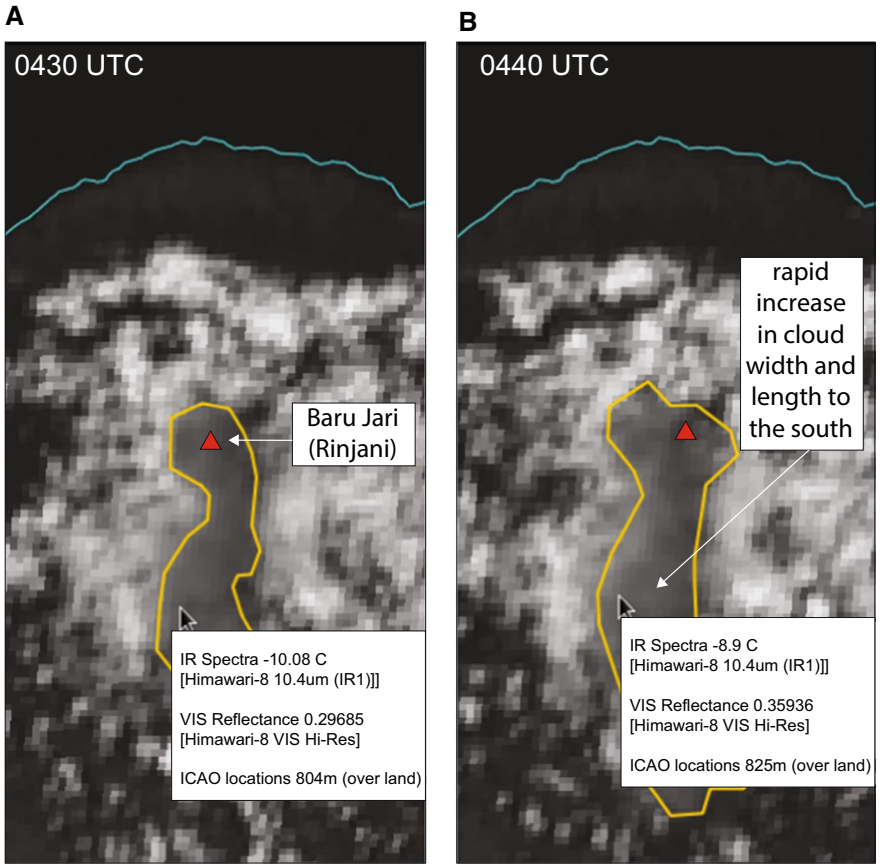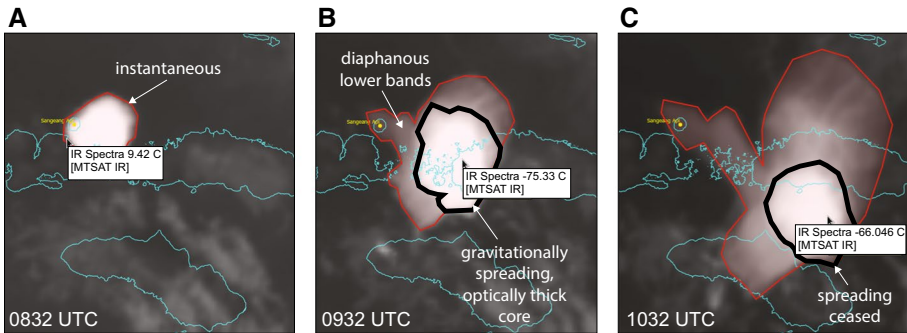
6.3.3 Sangeang Api

As we have described, the eruption of Sangeang Api should probably be considered instantaneous, as the eruption had ceased, with the cloud propagating away from the vent between the first and second satellite acquisitions (Fig. 10). We thus have no comparison of MER for this event. The cloud dispersion was also unusual, as the cloud had a high, optically thick core that changed little in size, with more diaphanous, lower bands pulled from it in different directions at different levels. It is likely that the core was the only part that was gravitationally spreading, and that for only a short time, as the more diaphanous bands were likely pulled from it by wind. By the third satellite acquisition the core had ceased to spread, and thus the estimate of mass is based on the initial spread. The estimated DRE volume of 0.3 km^3 is large, and we await future field workers' estimates of the volume of the deposit with which to compare this value. Given that the edge of the plume was often defined at a warm, low elevation, the contrast in density difference between plume top and intrusion edge (Eqs. 12, 13), results in a high initial mean particle concentration, which could result in an overestimate of deposit volume.

6.3.4 Manam

For Manam (2015), umbrella_MER estimates are at least an order of magnitude higher than any of the rise height methods (Fig. 8d). This was one of the eruptions for which the cloud size was estimated manually (Fig. 11). The edge defined by the observer was very warm and low, yielding an estimate of umbrella cloud depth of c. 10 km. Given that contrast in difference between plume top and intrusion edge (Eqs. 12, 13), the result is a large difference between cloud bulk density and gas density, hence a very high initial mean particle concentration in the volcanic cloud c. 0.5 kg m^3 (0.5 mg cm^3), the highest estimated in the present study.

For Manam (2004), average umbrella_MER estimates are consistent with rise height-method estimates (Fig. 8e), suggesting no unusual activity and stable atmospheric conditions. However, the umbrella_MER outputs do show a great variability, and even some instances of explosive growth or alternately cloud shrinking, causing an unphysical decrease in MER (Eq. 3). Careful analysis of the satellite imagery and APES-identified

A 0430 UTC

Baru Jari
(Rinjani)

IR Spectra -10.08 C
[Himawari-8 10.4um (IR1)]]

VIS Reflectance 0.29685
[Himawari-8 VIS Hi-Res]

ICAO locations 804m (over land)

B 0440 UTC

rapid
increase
in cloud
width and
length to
the south

IR Spectra -8.9 C
[Himawari-8 10.4um (IR1)]]

VIS Reflectance 0.35936
[Himawari-8 VIS Hi-Res]

ICAO locations 825m (over land)

C 1e7   Time vs. MER of particles

Rapid increase in
size and transition
to downwind
plume

MER of particles (kg/s)

Time (s)

Fig. 10 **a** Initial MTSAT-2 retrieval for the initiation of the Sangeang Api 30 May 2014 (0832 UTC) eruption; **b** second MTSAT-2 retrieval Sangeang Api eruption depicting the optically thick core and associated diaphanous lower bands (0932 UTC); **c** third MTSAT-2 retrieval for the Sangeang Api eruption depicting cessation of spreading (1032 UTC)
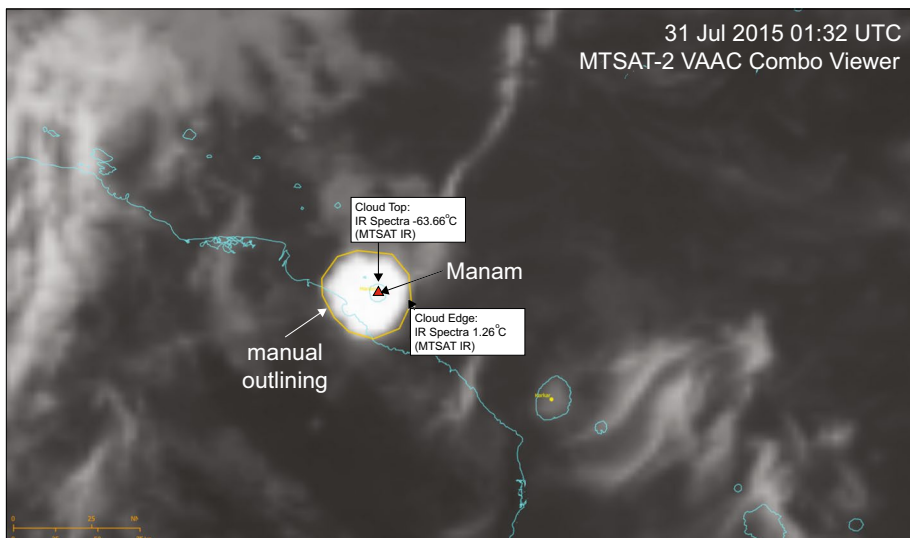
Fig. 11 MTSAT-2 retrieval for the initiation of the Manam (2015) eruption (0132 UTC 31 July 2015) featuring the manually delineated cloud edges

cloud suggests that the algorithm was confused by shearing of the margins of the cloud, as it drifted away from the volcano (Fig. 12). At 0325 UTC, the uniformly high, umbrella cloud, detached from the volcano, appears to be sheared towards the southwest, yielding a slightly diaphanous, striated cloud at variable but slightly lower level in that direction. This sheared portion of the cloud is incorporated by APES, although at 0225 UTC, it has not yet differentiated itself from the main cloud mass. The result is a near-doubling in cloud area between 0225 and 0325 UTC. At 0425 UTC, the sheared portion of the cloud has descended and differentiated itself from the main, high umbrella, and much of it has fallen below the algorithmic cut-off; thus, between 0325 and 0425 UTC, the cloud size
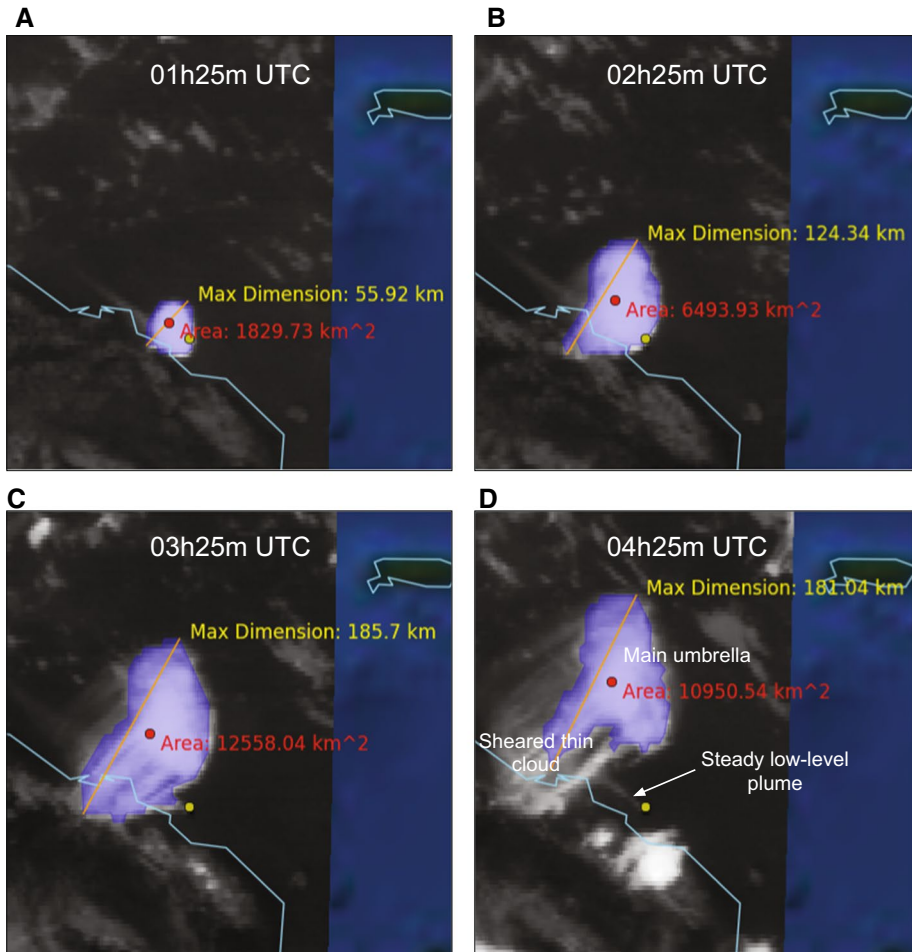
Fig. 12 MTSAT-2 retrieval and APES-identified clouds for initial stages of the Manam 27 January 2005 eruption; **a** 0125 UTC retrieval; **b** 0225 UTC retrieval; C. 0325 UTC retrieval featuring sheared portion of the cloud is incorporated by APES algorithm and D. 0425 UTC retrieval depicting that the sheared portion of the cloud has descended and differentiated itself from the main high umbrella

decreased according to APES. The result of these processes is a more variable MER with umbrella_MER.

For Manam (2005), umbrella_MER estimates are higher than are those for the rise-height-derived methods (Fig. 8f). The APES determined cloud areal growth was particularly rapid, resulting in high estimates of MER for umbrella_MER. There is some chance that the discrepancy between umbrella_MER and rise height methods might be related to confusion of the APES algorithm by high meteorological clouds particularly on the southeast side of the umbrella cloud. It is important to point out, that alone among the eruptions studied herein, the empirical method yielded MER estimates below those for PlumeRise and Plumeria. Based on Rule of Thumb (4), it should be considered whether this is the result of wind ingestion by the rising eruption column, and ash from the eruption was known to be rapidly dispersed at mid-tropospheric levels. Given the extreme rise

Fig. 13 **a** Himawari-8 retrieval for 2100 UTC during the Tinakula 1 eruption; **b** Himawari-8 retrieval for ▶
2130 UTC during the Tinakula 1 eruption; **c** Himawari-8 retrieval for 2150 UTC during the Tinakula 1
eruption featuring APES assimilation of first small convective cloud and; **d** Himawari-8 retrieval for 2210
UTC during the Tinakula 1 eruption featuring APES assimilation of second larger convective cloud

height (21–24 km), rapid growth and Rule of Thumb (6), the higher MER of umbrella_
MER, PlumeRise and Plumeria may be closer to reality.

6.3.5 Tinakula

For Tinakula 1 and 2, the rise height methods yield estimates of MER that are close to
those of umbrella_MER (Fig. 8g, h). This suggests that, in general, it was not too windy nor
too humid to cause difficulties in any of the methods. There are exceptions to the overall
good correspondence. These occur at the beginning of the eruption pulses, and during the
Tinakula 1 pulse. At the beginning of the pulses, the difference could be related to the
rapid cloud growth at the beginning of an event related to momentum-driven coupled with
gravity-driven flow (Pouget et al. 2016). It might alternatively relate to a decreasing MER
with time, which could not be resolved in any of the plume height-derived models due
to persistence of the initial, high-level cloud obscuring a cloud top. An anomalously high
speed would result in too high an estimate of MER for the umbrella_MER method. We
note that this is perhaps a general feature of the umbrella_MER calculations and suggest
that a goal of future work might be to explicitly model the early, momentum-driven flow
and explore the likelihood of an obscured, descending cloud top. The other discrepancy
between methods is almost certainly caused by assimilation of two convective clouds by
APES during the Tinakula 1 pulse. The first jump in MER (Fig. 13) occurs just as a small
convective cloud of similar height is assimilated by APES into the growing volcanic cloud
(Fig. 13). The second, larger jump, in MER occurs as the volcanic cloud assimilates a
second, larger convective cloud. There is no doubt, therefore, that these jumps in MER are
artefacts of the algorithm and represent a difficulty that should be addressed in future.

6.3.6 Further reflections

As noted in Rule of Thumb (2), in a moist atmosphere, when air is saturated and
conditionally unstable, lower or near zero MER plumes can rise to a height determined
by atmospheric, not source, conditions, so the empirical method could yield too high an
estimate of MER (Tupper et al. 2009). At the same time, the sensitivity of MER estimated
by PlumeRise and Plumeria to rise height should be weaker than normal [Rule of Thumb
(3)], and umbrella_MER could yield too high an estimated MER. We can see these
general trends in the results, in that both the empirical method and umbrella_MER tend to
overestimate MER (Figs. 8, 14). At the same time, the difference between the PlumeRise
and the Plumeria estimates of MER can be quite variable.

The opposite situation occurs in high wind [Rules of Thumb (4) and (5)]. Use of the
empirical method can result in estimates of MER that are too low, because the more rapid
entrainment due to wind results in a plume reaching a lower rise height than would occur
in a still atmosphere, so the estimated MER is low. This problem should be particularly
characteristic in the empirical method but could occur in the numerical methods.
Nevertheless, umbrella_MER could find that a larger amount of mass is going into the
downwind plume if it spreads laterally at a high rate, and the estimate of MER should
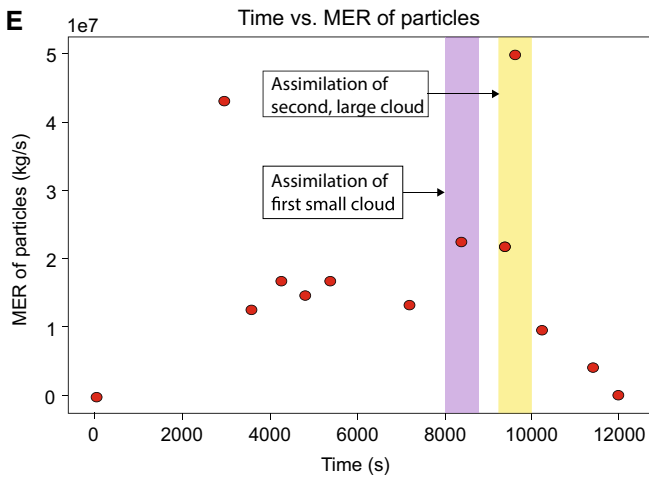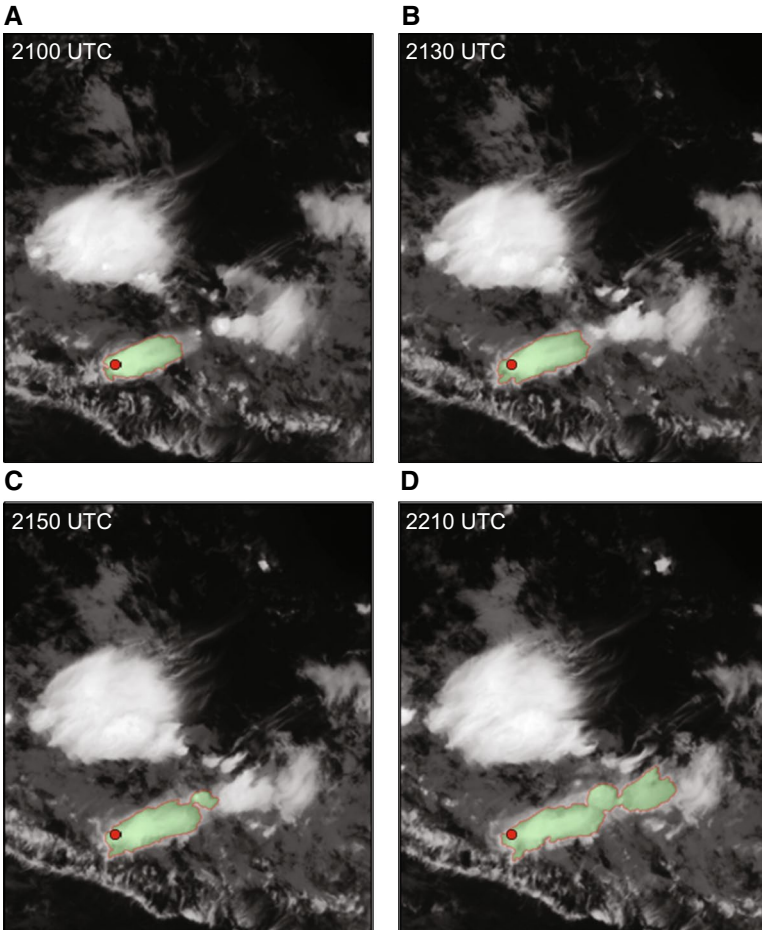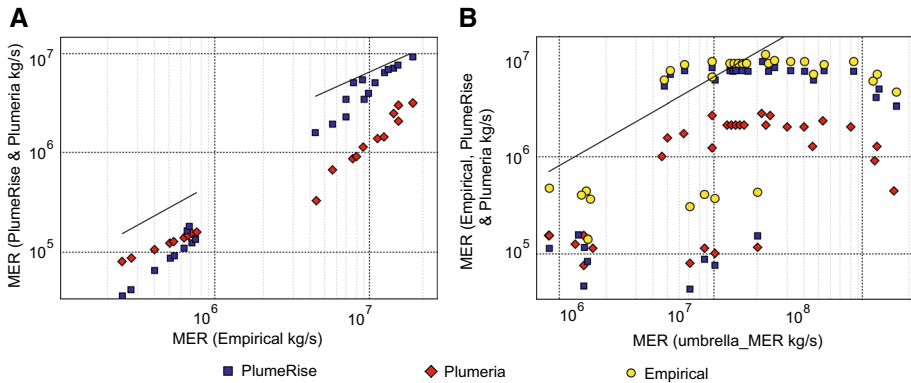
Fig. 14 Comparison of MER estimates by technique; **a** empirical method MER (kg s^{-1}) 'Mastin' (2009) numerical fitting parameters versus Plumeria (kg s^{-1}) and PlumeRise (kg s^{-1}); **b** umbrella_MER (kg s^{-1}) versus empirical method (kg s^{-1}), PlumeRise (kg s^{-1}) and Plumeria (kg s^{-1})

be higher. An example of this might be the Manam 2005 event for which umbrella_MER yielded a MER > 150% of that for the empirical model, which yielded the lowest estimates of MER.

Figure 14 shows a summary comparison of MER estimates among the different models. Figure 14a shows that MER estimates from PlumeRise, Plumeria and the empirical estimates can vary considerably, reflecting the variability in characterisation of the critical atmospheric parameters of wind and water vapour. However, because of the similarity in underlying physics, there is a high correlation between any two methods for a given eruption. The empirical method consistently yields higher estimates of MER than do either of the numerical methods [Rule of Thumb (2)—the atmosphere is moist]. At high MER, PlumeRise tends to be more consistent with the empirical method, whereas at low MER, PlumeRise tends to be more consistent with Plumeria. Figure 14b shows that MER estimates from umbrella_MER are quite different from those for the rise height methods, reflecting the difference in data and physics that goes into the calculation. Umbrella_MER estimates are generally higher than are the rise height estimates of MER. The generally higher MER estimates for umbrella_MER may relate to a number of persistent features: (1) overestimate of bulk density due to the operator drawing the plume edge at high brightness temperature/low altitude and; (2) plumes rising to the tropopause and stopping [Rule of Thumb (6)] despite having more mass and energy to rise higher. Such plumes will still spread radially at a rate commensurate with the high mass flux. It is striking to note that the lower MER of pyroclasts into the umbrella region estimated by umbrella_MER, as opposed to that from the vent estimated by the plume-rise methods [Rule of Thumb (1)], there are virtually no cases where this needs to be invoked. Being dependent on plume height, which remains relatively constant due to masking of a lowering plume, estimates from the rise height methods remain somewhat constant through time, whereas the umbrella_MER estimates vary, which may reflect the finer granularity in estimating source parameters that comes from monitoring horizontal cloud growth rate rather than a somewhat steady cloud top height.

The umbrella_MER technique, unlike the other umbrella cloud techniques used by Mastin et al. (2014), Hargie et al. (2019) and Costa et al. (2013), does not depend at all on rise height models or calculations. These previous works use a scaling from the rise height

models that umbrella_MER does not depend on; therefore they cannot be considered truly independent from the rise height calculation. Umbrella_MER provides a technique truly independent from rise height.

7 Conclusion

Identifying the spatial extent of volcanic ash clouds in the atmosphere and forecasting their direction and speed of movement has important implications for the safety of the aviation industry, community preparedness and disaster response at ground level. An automated statistics and physics-based algorithm, the Automated Probabilistic Eruption Surveillance (APES) algorithm was presented here for auto-detecting volcanic clouds in satellite imagery and distinguishing them from meteorological cloud in near real-time. Coupled with a gravity current model of early cloud growth, which uses the area of the volcanic cloud as the basis for mass measurements (umbrella_MER), the mass flux of particles into the volcanic cloud was estimated for a series of case study eruptions throughout the VAAC Darwin and VAAC Wellington areas of responsibility as a function of time. The evolution of each eruption was quantitatively characterised allowing for rapid estimation of source parameters used in volcanic ash transport and dispersion models.

For Kelud and Tinakula, MER estimated from umbrella_MER and rise height-based models were similar. Since the methods are quite different and dependent on different physical phenomena, this suggested that the MER estimates can be robust given good meteorological conditions, cloud visibility and consistent umbrella mapping. The differences in estimated MER between umbrella_MER and the rise height methods appear to be systematic, as the umbrella_MER estimates are consistently high relative to the rise height methods. When air is saturated and conditionally unstable, all plumes, no matter the MER below a certain limit, rise to a height determined by atmospheric, not source, conditions, so methods dependent on calculating MER from rise height yield too low an estimate of MER, whereas umbrella_MER does not, as its estimate is dependent on the estimated density (mass) anomaly in a growing umbrella cloud or downwind plume. When wind speed is high, rise height calculations can result in estimates of MER that are too low, because the more rapid entrainment due to the wind results in a plume reaching a lower rise height than would occur in a still atmosphere.

The umbrella_MER method is subject to its own shortcomings, such as the simplifications and shortcomings inherent in the model, and cloud mapping, particularly in relation to defining the cloud edge and the related calculation of densities. However, it has been demonstrated that the APES algorithm does a much better job of picking an appropriate cloud edge than does the manual approach. The fact that umbrella_MER manual estimates are always higher than other techniques is related to the estimation of a too warm, low edge to the cloud, and hence too high a particle concentration. The human observer could be trained to obtain a better result, but for now the algorithm is clearly superior, if matching of plume rise techniques is considered a measure of goodness.

Overall, a weighted multi-model approach is probably best in providing the most accurate estimate of MER and mass loading from volcanic eruptions. If developed fully, the combination of a quick, robust detection algorithm (APES) and mass loading estimation algorithm (umbrella_MER) could result in real-time estimates of early positions and masses of volcanic clouds for improved initialisation of volcanic ash transport and

dispersal models and the production of more representative (higher confidence) volcanic ash advisories of critical importance to the aviation industry.

Compliance with ethical standards

Conflict of interest The authors declare that they have no conflict of interest.

References

Bursik MI, Carey SN, Sparks RSJ (1992) A gravity current model for the May 18, 1980 Mount-St-Helens plume. Geophys Res Lett 19(16):1663–1666

Carey S, Sparks RSJ (1986) Quantitative models of the fallout and dispersal of tephra from volcanic eruption columns. Bull Volcanol. https://doi.org/10.1007/BF01046546

Chen JC (1980) Studies on gravitational spreading currents. Dissertation (Ph.D.), California Institute of Technology. https://resolver.caltech.edu/CaltechTHESIS:09302010-090407312

Christie DR, Kennett BL, Tarlowski C (2005) Detection of regional and distant atmospheric explosions at IMS infrasound stations. In: Proceedings of the 27th seismic research review: ground-based nuclear explosion monitoring technologies. Technical report LA-UR-05–6407, pp 817–827

Costa A, Folch A, Macedonio G (2013) Density-driven transport in the umbrella region of volcanic clouds: implications for tephra dispersion models. Geophys Res Lett 40(18):4823–4827

Costa A, Suzuki YJ, Cerminara M, Devenish BJ, Esposti Ongaro T, Herzog M, Van Eaton AR, Denby LC, Bursik M, de' Michieli Vitturi M, Engwell S, Neri A, Barsotti S, Folch A, Macedonio G, Girault F, Carazzo G, Tait S, Kaminski E, Mastin LG, Woodhouse MJ, Phillips JC, Hogg AJ, Degruyter W, Bonadonna C (2016) Results of the eruptive column model inter-comparison study. J Volcanol Geotherm Res 326:2–25

Global Volcanism Program (2013a) Kelut (263280) in Volcanoes of the world, v. 4.6.4. In: Venzke E (ed) Smithsonian Institution. https://dx.doi.org/10.5479/si.GVP.VOTW4-2013. http://volcano.si.edu/volcano.cfm?vn=263280. Downloaded 18 Jan 2018

Global Volcanism Program (2013b). Rinjani (264030) in Volcanoes of the world, v. 4.6.4. In: Venzke E (ed) Smithsonian Institution. https://dx.doi.org/10.5479/si.GVP.VOTW4-2013. http://volcano.si.edu/volcano.cfm?vn=264030. Downloaded 18 Jan 2018

Global Volcanism Program (2013c) Sangeang Api (264050) in Volcanoes of the world, v. 4.6.4. In: Venzke E (ed) Smithsonian Institution. https://dx.doi.org/10.5479/si.GVP.VOTW4-2013. http://volcano.si.edu/volcano.cfm?vn=264050. Downloaded 18 Jan 2018

Global Volcanism Program (2013d) Manam (251020) in Volcanoes of the world, v. 4.6.4. In: Venzke E (ed) Smithsonian Institution. https://dx.doi.org/10.5479/si.GVP.VOTW4-2013. http://volcano.si.edu/volcano.cfm?vn=251020. Downloaded 18 Jan 2018

Global Volcanism Program (2013e) Tinakula (256010) in Volcanoes of the world, v. 4.6.4. In: Venzke E (ed) Smithsonian Institution. https://dx.doi.org/10.5479/si.GVP.VOTW4-2013. http://volcano.si.edu/volcano.cfm?vn=256010. Downloaded 18 Jan 2018

Hargie KA, Van Eaton AR, Mastin LG, Holzworth RH, Ewert JW, Pavolonis M (2019) Globally detected volcanic lightning and umbrella dynamics during the 2014 eruption of Kelud, Indonesia. J Volcanol Geotherm Res 382:81–91

Holasek RE, Woods AW, Self S (1996) Experiments on gas-ash separation processes in volcanic umbrella plumes. J Volcanol Geotherm Res 70(3–4):169–181

Johnson CG, Hogg AJ, Huppert HE, Sparks RSJ, Phillips JC, Slim AC, Woodhouse MJ (2015) Modelling intrusions through quiescent and moving ambients. J Fluid Mech 771:370–406

Kotsovinos NE (2000) Axisymmetric submerged intrusion in stratified fluid. J Hydraul Eng 126(6):446–456

Kristiansen N, Prata F, Stohl A, Carn SA (2015) Stratospheric volcanic ash emissions from the 13 February 2014 Kelut eruption. Geophys Res Lett 42:588–596. https://doi.org/10.1002/2014GL062307

Lemckert CJ, Imberger J (1993) Axisymmetric intrusive gravity currents in linearly stratified fluids. J Hydraul Eng 119:662–679

Maeno Fukashi, Nakada Setsuya, Yoshimoto Mitsuhiro, Shimano Taketo, Hokanishi Natsumi, Zaennudin Akhmad, Iguchi Masato (2019) A sequence of a plinian eruption preceded by dome destruction at Kelud volcano, Indonesia, on February 13, 2014, revealed from tephra fallout and pyroclastic density current deposits. J Volcanol Geotherm Res 382:24–41. https://doi.org/10.1016/j.jvolgeores.2017.03.002

Mastin LG, Guffanti M, Servranckx R, Webley P, Barsotti S, Dean K, Durant A, Ewert JW, Neri A, Rose WI, Schneider D, Siebert L, Stunder B, Swanson C, Tupper A, Volentik A, Waythomas CF (2009) A multidisciplinary effort to assign realistic source parameters to models of volcanic ash-cloud transport and dispersion during eruptions. J Volcanol Geotherm Res 186(1–2):10–21

Mastin LG, Van Eaton AR, Lowenstern JB (2014) Modeling ash fall distribution from a Yellowstone supereruption. Geochem Geophys Geosyst 15(8):3459–3475

Pavolonis MJ, Feltz WF, Heidinger AK, Gallina GM (2006) A daytime complement to the reverse absorption technique for improved automated detection of volcanic ash. J Atmos Ocean Technol 23:1422–1444

Pouget S, Bursik M, Webley P, Dehn J, Pavolonis M (2013) Estimation of eruption source parameters from umbrella cloud or downwind plume growth rate. J Volcanol Geotherm Res 258:100–112

Pouget S, Bursik M, Johnson CG, Hogg AJ, Phillips JC, Sparks RSJ (2016) Interpretation of umbrella cloud growth and morphology: implications for flow regimes of short-lived and long-lived eruptions. Bull Volcanol 78(1):1

Prata F, Woodhouse M, Huppert HE, Prata A, Thordarson T, Carn S (2017) Atmospheric processes affecting the separation of volcanic ash and SO_2 in volcanic eruptions: inferences from the May 2011 Grímsvötn eruption. Atmos Chem Phys 17(17):10709–10732

Sparks RSJ, Bursik MI, Carey SN, Gilbert JS, Glaze LS, Sigurdsson H, Woods AW (1997) Volcanic plumes. Wiley, New York

Suzuki YJ, Koyaguchi T (2009) A three-dimensional numerical simulation of spreading umbrella clouds. J Geophys Res Solid Earth 114:B03209. https://doi.org/10.1029/2007JB005369

Tupper A, Itikarai I, Richards M, Prata F, Carn S, Rosenfeld D (2007) Facing the challenges of international airways volcano watch: the 2004/05 eruption of Manam, Papua New Guinea. Weather Forecast 22(1):175–191

Tupper A, Textor C, Herzog M, Graf HF, Richards MS (2009) Tall clouds from small eruptions: the sensitivity of eruption height and fine ash content to tropospheric instability. Nat Hazards 51(2):375–401

VAAC Darwin (2014a) Kelud—13 February 2014 post event report (external), Volcanic Ash Advisory Centre (Darwin). Australian Bureau of Meteorology, Melbourne

VAAC Darwin (2014b) Sangeang Api—30 May 2014 post event report (external). Volcanic Ash Advisory Centre (Darwin), Australian Bureau of Meteorology, Melbourne

VAAC Darwin (2015) Manam—31 July 2015 post event report (external). Volcanic Ash Advisory Centre (Darwin), Australian Bureau of Meteorology, Melbourne

VAAC Darwin (2016) Rinjani—1 August 2016 post event report (external). Volcanic Ash Advisory Centre Darwin, Australian Bureau of Meteorology, Melbourne

Wilson L, Sparks RSJ, Huang TC, Watkins ND (1978) The control of volcanic column heights by eruption energetics and dynamics. J Geophys Res (Solid Earth) 83(B3):1829–1836

Woodhouse MJ, Hogg AJ, Phillips AC, Sparks RSJ (2013) Interaction between volcanic plumes and wind during the 2010 Eyjafjallajökull eruption, Iceland. J Geophys Res (Solid Earth) 118(1):92–109

Woods AW, Kienle J (1994) The dynamics and thermodynamics of volcanic clouds: theory and observations from the April 15 and April 21, 1990 eruptions of redoubt volcano, Alaska. J Volcanol Geotherm Res 62(1–4):273–299. https://doi.org/10.1016/0377-0273(94)90037-X

Affiliations

Adele Bear-Crozier[1] [ID] **· Solène Pouget[2] · Marcus Bursik[2] · Emile Jansons[1] · Jarrad Denman[1] · Andrew Tupper[2] · Rose Rustowicz[2]**

[1] Volcanic Ash Advisory Centre (Darwin), Bureau of Meteorology, Melbourne, Australia

[2] Department of Geology, University at Buffalo, SUNY, Buffalo, NY 14260, USA